Thermal analysis

The Du Pont Model 900 differential thermal analyzer was used with the standard DTA cell and the DSC cell[11] (this is actually a DTA cell: it has a quantitative potential not available in the standard cell and differs from the latter in that the thermocouple is not in direct contact with the sample). Glass beads were used as reference material in the former, and an empty pan for the latter. Unless otherwise indicated a gas flow of 100 ml min^{-1} was maintained in the DSC cell, a static atmosphere in the DTA cell, and a nominal heating rate of 20°C min^{-1} in both.

The sample yarn or fiber was wound closely and tightly around the chromel: alumel thermocouple, so that when it was inserted in the glass melting point tube in the DTA cell, the sample space was well filled. This was not possible with the coarse Saran monofilament, which was cut into short (2–3 mm) lengths which were tightly packed into the tube to form a bundle into which the thermocouple was forced.

Material for the DSC cell was cut into 3 mm square specimens, or the yarn was cut into short (ca. 2 mm) lengths, and packed in the aluminium pans. The pan lids were inverted to minimise head space and to pack the sample firmly to the base of the pan to obtain good thermal contact. The normal pan lid does not allow significant pressure build-up or pan distortion unless there is rapid gas evolution, since it does not fit tightly unless crimped. However, in some cases perforated lids were used to allow easier efflux of evolved products, and for these four 0.5 mm holes were pierced through the normal lid.

A sample mass of 2–4 mg was used in the DSC cell and about 2 mg in the standard cell, the instrument response was very similar in either cell.

RESULTS AND DISCUSSION

The DTA curves for PVC powder, obtained under various conditions, are shown (Fig. 1) for the range 100–400°C. The dehydrochlorination of PVC is accompanied by a mass loss of the order of 60% of the original weight, and the formation of a carbonaceous foamed char which undergoes further reaction. The factors, particularly thermal resistance, determining the performance of idealised DTA and DSC apparatus have been described[17]. In the standard (Du Pont) DTA cell, the sensing thermocouple is in direct contact with the sample, and foaming decomposition can cause fluctuating thermal contact, and hence an erratic and irreproducible DTA curve. The changing baseline thus compounds the reported difficulty of interpretation of DSC curves of decomposing fibers[8]. As a consequence the curves obtained in the standard cell at temperatures beyond the initial major decomposition have limited utility, and comparison between curves obtained on the standard and DSC cells above the decomposition should be treated with care.

The DTA curve of PVC powder in the standard cell (Fig. 1, f) comprised a small endothermic baseline shift at 250°C prior to a broad endotherm from 250–350°C, peaking at 305°C, and an exothermic trend on further decomposition. The small endothermic shift was not evident in curves obtained on the DSC cell and was

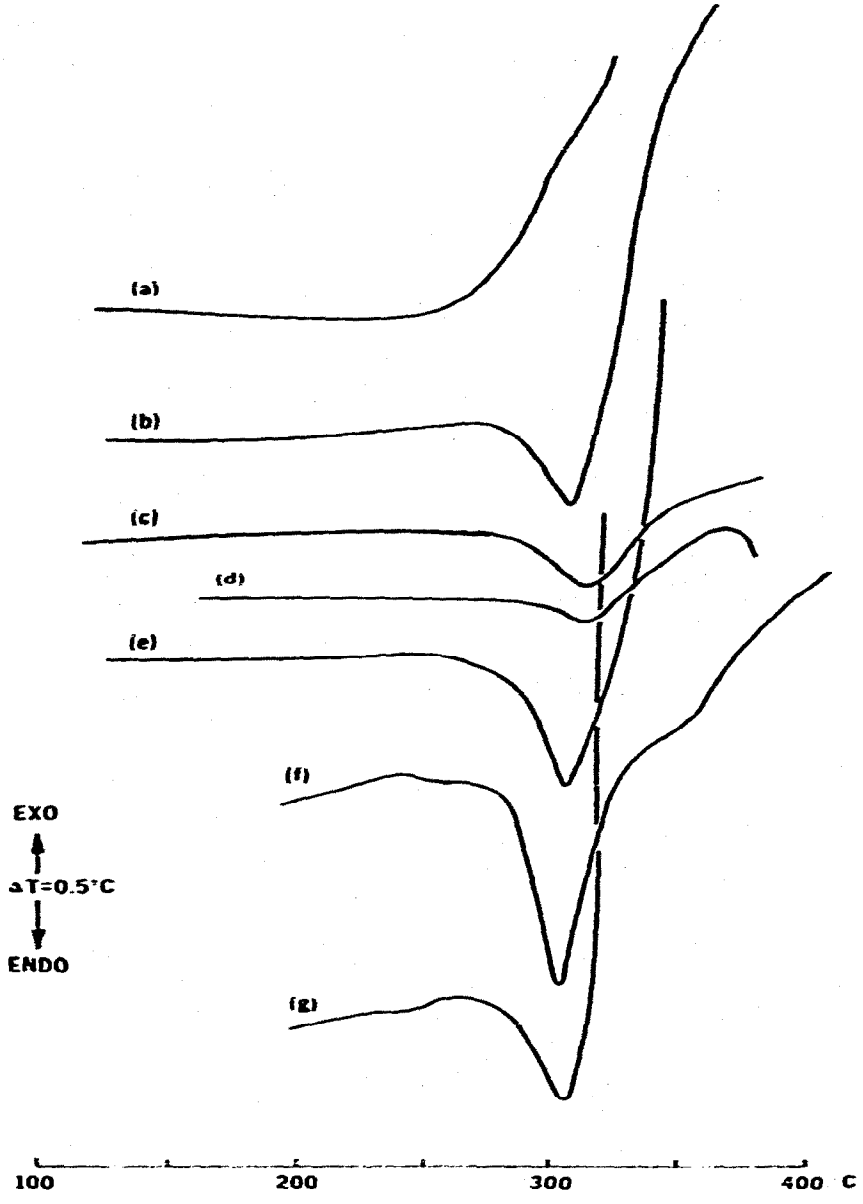

Fig. 1. DTA curves of PVC powder, heating rate 20°C min^{-1}. (a) = DSC cell, open pan, in air; (b) = DSC cell, perforated lid, in air; (c) = DSC cell, perforated lid, in N_2; (d) = DSC cell, open pan, in N_2; (e) = DSC cell, closed lid, in N_2; (f) = DTA cell; (g) = DTA cell, contains sliver of DSC pan.

assumed to result from a sintering of the powder onto the thermocouple. The curve obtained for the DSC cell, using a closed sample pan in nitrogen (Fig. 1, e) showed a relatively small endothermic peak followed by a vigorous exotherm, before deformation of the pan caused an irregular trace. When the product gases were allowed to diffuse from the pan, using either a perforated pan lid or no pan lid (Fig. 1, c and d, respectively) the exothermicity of the reaction was much reduced. In an open pan

in air (Fig. 1, a) reaction was apparent at a lower temperature than in nitrogen and was exothermic from the start, while under conditions of limited access of air using a perforated lid (Fig. 1, b) an initial net endotherm was followed by a vigorous exotherm. Finally, when a sliver of DSC pan was included in the DTA sample tube with the PVC, a vigorous exotherm followed the initial endothermic reaction (Fig. 1, g).

Reaction in air in an open pan of either platinum or aluminium gave a DTA curve which was qualitatively the same; under these conditions the DTA curve (Fig. 1, a) obtained in an aluminium pan, therefore, represents a predominantly oxidative decomposition. It seems probable that the corresponding curve in nitrogen (Fig. 1, d) represents predominant thermal decomposition. The standard DTA cell is characterised by an unusually high degree of product retention[18], so that the decomposition takes place in a self-generated atmosphere, and under these conditions is more endothermic. The contrast between DTA curves (Fig. 1, f and g) in the presence and absence of aluminium demonstrates the potential for interaction between sample, or decomposition products, and the container. The initial exotherm in the closed pan (Fig. 1, e) is believed to be due to such an interaction with the pan; although other explanations are possible, for it is known that the evolution of large volumes of gas can cause irreproducible DTA traces[19], and deformation of the sample pan can cause spurious DTA peaks.

The autocatalytic effect of evolved hydrogen chloride, and the modification of the DTA curves of PVC by the presence of additives and plasticizers has been shown[9]. Thus the curves shown in Fig. 1 are not necessarily representative of processed material which may differ in both composition, and particle size (ease of diffusion of product from the material), nonetheless the same factors will be operative and the DTA curve will be determined by procedural variables.

For Saran the differences between the DTA curves obtained in the two cells were less obvious (Fig. 2). The melting was clearly shown in a broad endotherm peaking at about 170°C, in good agreement with the reported value of 170–175°C for the semi-crystalline vinylidine chloride/vinyl chloride copolymers[16]. Curves obtained in the DTA cell (Fig. 2, c and d) showed an irregularity between 220–270°C, the range over which Saran was observed to decompose with extensive gas evolution. The decomposition was only slightly endothermic and was manifested in the DTA curves by the variable thermal contact causing an irregular trace. In the DSC cell, using a perforated lid in nitrogen, this decomposition was not detected, but vigorous exothermic reaction was evident above 250°C (Fig. 2, b). This could be due to the aluminium pan; although the presence of a sliver of aluminium with the sample in the DTA cell resulted in an increased exotherm, the effect was evident at a higher temperature (Fig. 2, c). In the DSC cell the exothermic decomposition was evident at slightly lower temperatures in air than it was in nitrogen (Fig. 2, a and b).

The DTA curves of the polyblend Cordelan (Fig. 3), showed a broad endotherm at 200–220°C. This endotherm was found to be insensitive to changes of heating rate (5–40°C min^{-1}). As the disorientation of crystallites in poly(vinyl alcohol), and the melting point of formalised poly(vinyl alcohol) fibres[20] commonly occur in this

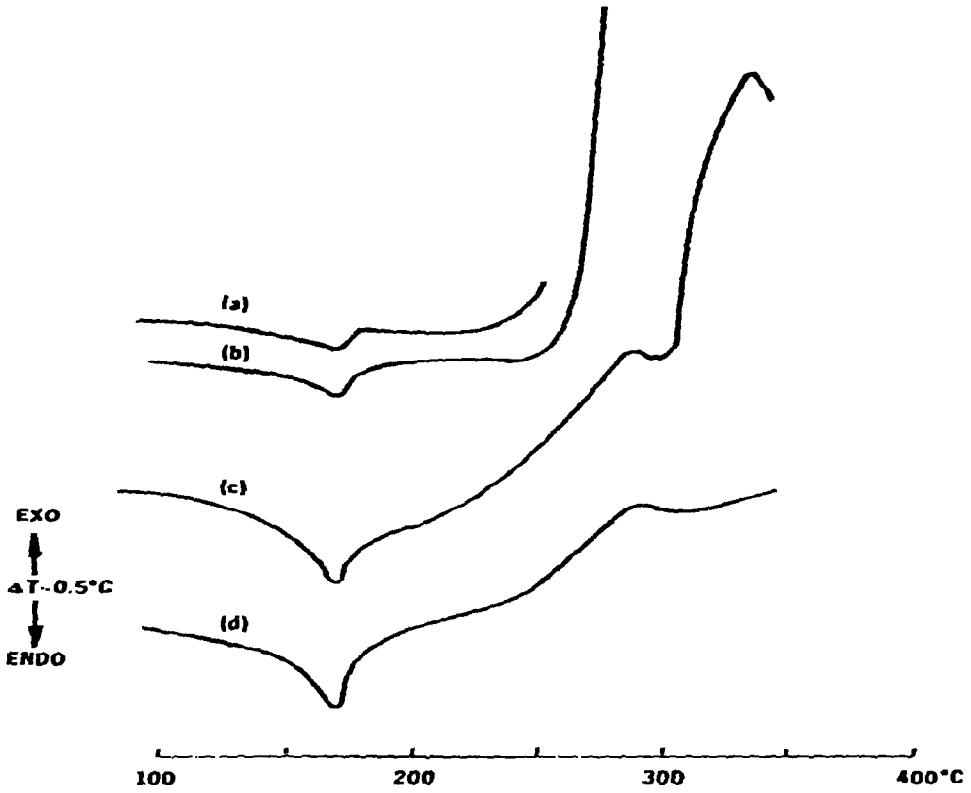

Fig. 2. DTA curves of Saran monofilament, heating rate 20°C min^{-1}. (a) = DSC cell, perforated lid, in air; (b) = DSC cell, closed lid, in N_2; (c) = DTA cell, with sliver of DSC pan; (d) = DTA cell.

range[10], this endotherm in the DTA curve of Cordelan can be attributed to the poly(vinyl alcohol) crystallinity. The subsequent decomposition of Cordelan can be interpreted as either a multistage exothermic reaction, or, more probably, concurrent endothermic and exothermic reactions, near 300°C. The DTA curves of the polyblend had little, if any, resemblance to those of the component polymers except for the PVA crystallite disorientation endotherm (Fig. 3, a, b and c). The degree of product restraint affected the DTA curve (Fig. 3, c and d); reaction occurred at a lower temperature in a closed pan than in one with a perforated lid, and the relative balance of the two reactions was changed. The curve obtained in the standard cell (Fig. 3, e) was substantially different and gave clear separation of an endothermic and an exothermic reaction. Under oxidising conditions both reactions were suppressed in favour of a more general exotherm (Fig. 3, f).

In contrast to the previous materials the modacrylic fibers, Kanekalon and Teklan, gave DTA curves that were not sensitive to the different conditions in the two cells. For Kanekalon (Fig. 4) there was no qualitative difference between curves obtained in air or nitrogen in the DSC cell, or under product restraint in the DTA cell. Teklan (Fig. 5), on the other hand, was slightly more sensitive to oxidation and an

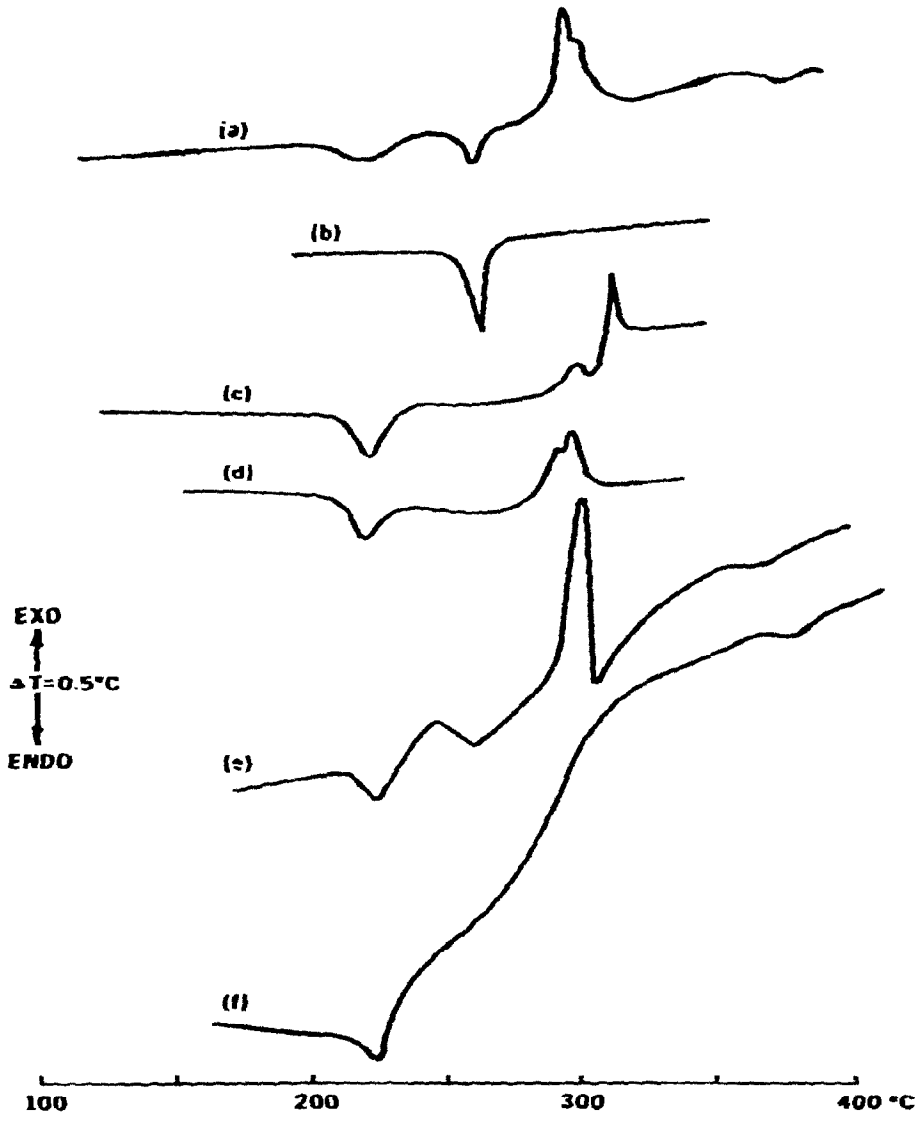

Fig. 3. DTA curves of Cordelan; heating rate 20 °C min^{-1}. (a) = Cordelan/polyethylene terephthalate, DSC cell, perforated lid, in N_2; (b) = Polyester, DSC cell, perforated lid, in N_2; (c) = Cordelan, DSC cell, perforated lid, in N_2; (d) = Cordelan, DSC cell, closed lid, in N_2; (e) = Cordelan, DTA cell; (f) = Cordelan, DSC cell, perforated lid, in air.

endotherm was suppressed in the DTA curve under conditions of reasonable air access.

The DTA curves of both modacrylics were characterised by small melting endotherms at 190–200°C, which were insensitive to change of heating rate (5–40°C min^{-1}). After melting of the semicrystalline region each fibre underwent endothermic decomposition, peaking near 250°C (Teklan) and 290°C (Kanekalon), and then a

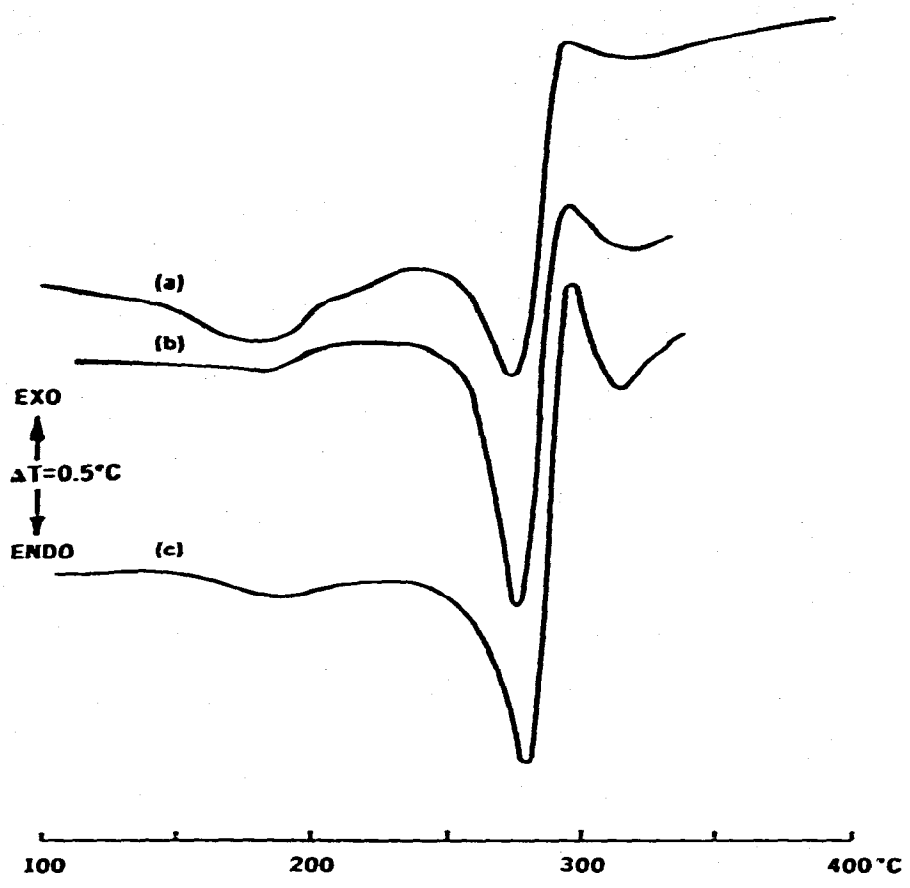

Fig. 4. DTA curves of Kanekalon, heating rate, 20°C min^{-1}. (a) = DTA cell; (b) = DSC cell, perforated lid, in N_2; (c) = DSC cell, perforated lid, in air.

vigorous exotherm, peaking at 280–290°C and 295–300°C, respectively. The endothermic decompositions thus bear a superficial resemblance to the decomposition of Saran and PVC, respectively, while the exotherms are similar to those of acrylonitrile homopolymer[21] and acrylic fibers[4], and, in contrast to a previous report[8], under these conditions the DTA curves of the modacrylics are not dominated by a resemblance to the chlorohomopolymer. The reactions are dependent on heating rate and the balance of exotherm and endotherm can be substantially altered by suitable choice of rate*; this may be utilised in identification.

The DTA curve of the Teklan/Celon fabric obtained at 20°C min^{-1} in the DSC cell (Fig. 6, a) differed from those of the component fibers (Fig. 5, c; Fig. 6, d); the 250°C endotherm was not evident. The curve obtained in the DTA cell (Fig. 6, c) at 20°C min^{-1} was reasonably additive, although some lowering of the Celon melting

* A fiber identified only as a chlorine containing modacrylic was found (DSC cell closed pan) to have m.p. 210°C, and an exothermic peak at 300°C, at a heating rate of 20°C min^{-1}; at 100°C min^{-1}, there was an additional endotherm peaking at 310°C, and the exothermic peak had shifted to 340°C.

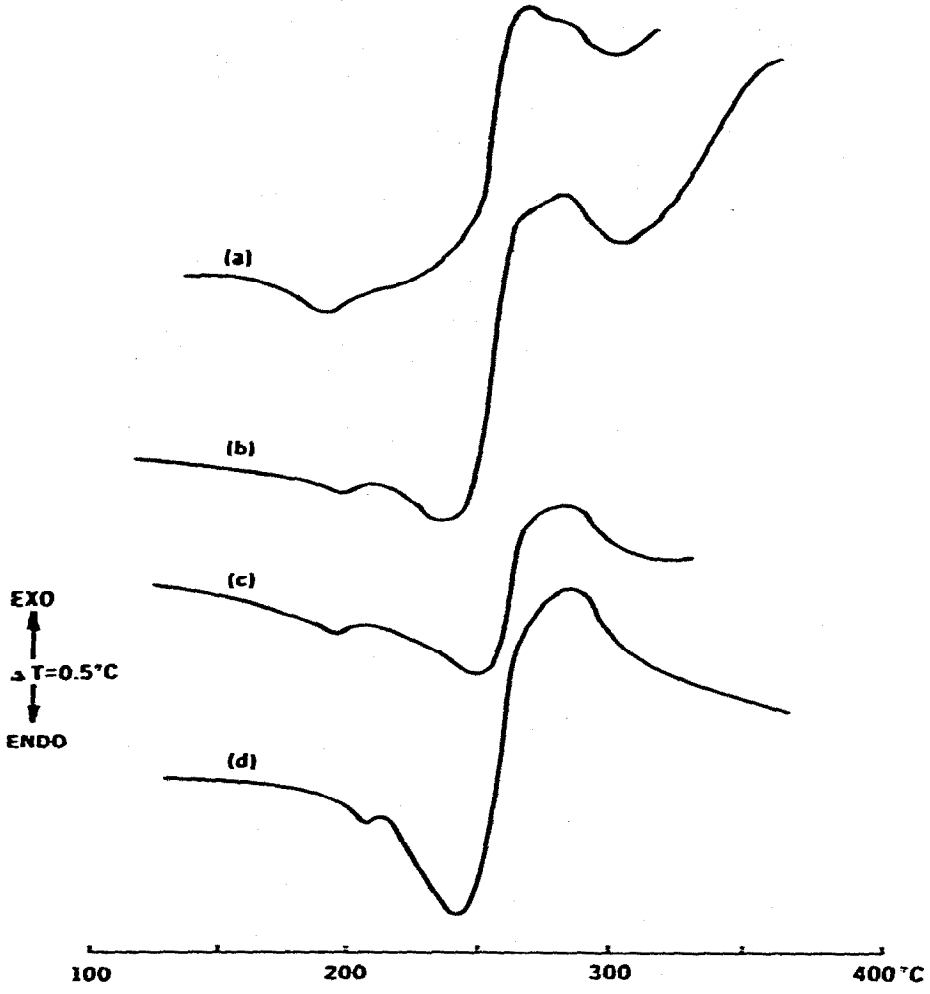

Fig. 5. DTA curves of Teklan; heating rate 20°C min^{-1}. (a) = DSC cell; perforated lid in air; (b) = DSC cell; closed lid, in air; (c) = DSC cell; perforated lid, in N_2; (d) = DTA cell.

was evident. At higher heating rates the characteristics of both fibers are again shown in curves obtained in the DSC cell (Fig. 6, b).

In contrast to those of the Teklan/Celon fabric, the DTA curves of the Teklan/cotton blend showed no qualitative difference from those of Teklan alone, except for a dehydration endotherm near 100°C. Cotton presents a relatively uneventful thermogram in this temperature range (150–350°C) on this equipment.

The Cordelan/poly(ethylene terephthalate) (PET) fabric gave a DTA curve in the DSC cell (Fig. 3, a) which showed the melting of the PET (Fig. 3, b) as well as that of Cordelan, and although the reaction exotherm of the Cordelan was slightly modified by the presence of the other fiber, it remained distinctive.

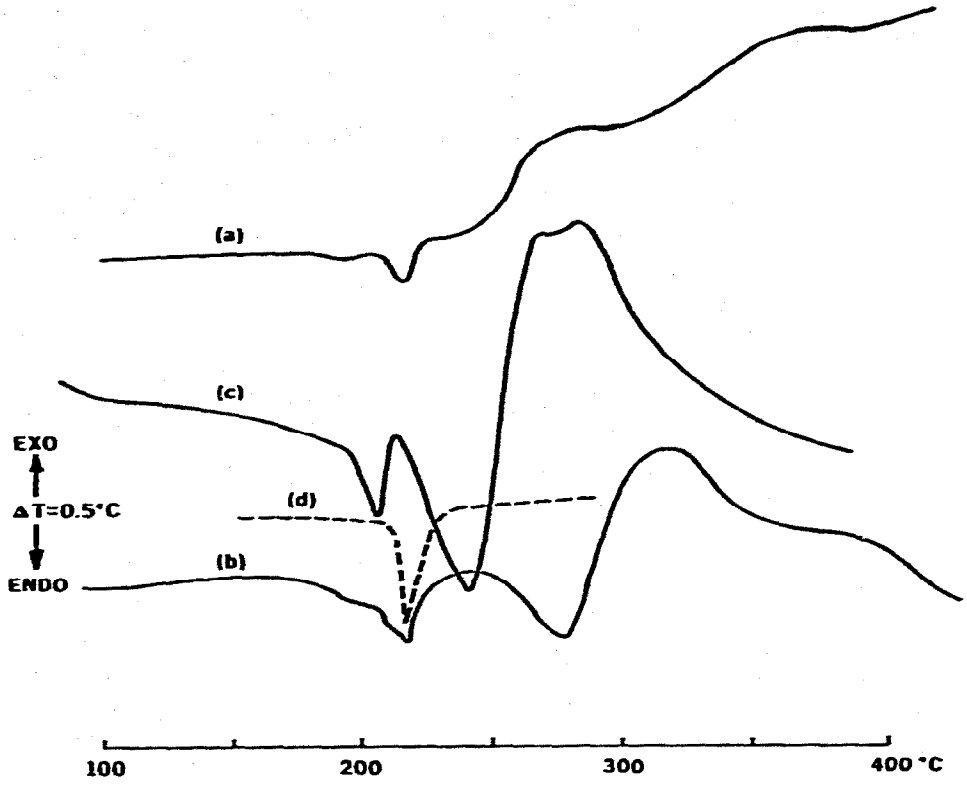

Fig. 6. DTA curves of Teklan/Celon. (a) = DSC cell, perforated lid, in N_2, 20°C min^{-1}; (b) = DSC cell, perforated lid, in N_2, 100°C min^{-1}; (c) = DTA cell, 20°C min^{-1}; (d) = *Celon*, DSC cell, perforated lid, in N_2, 20°C min^{-1}.

CONCLUSIONS

There is a continual need for an awareness of the procedural nature of DTA and DSC results. The foregoing can be explained in terms of cell geometry and construction affecting the interaction of sample, product and container.

During decomposition reactions there are major changes in the mass, size, shape, heat capacity and thermal transfer properties of the sample, which result in changes in the baseline of DTA and DSC curves[17]. This complicates interpretation of the curves over extended decomposition and temperature ranges and between different instruments. The present work has shown differences between the Du Pont DSC and DTA cells. Bingham and Hill[8], in studies which included some chlorofibers and modacrylics under somewhat similar conditions (the extent of diffusion through their perforated sample pan lids cannot be assessed, since no detail is given, but it seems probable that there is an effective self-generated atmosphere) obtained curves which show significant differences to the present results, in terms of apparent general exothermicity.

In the present case, it has not proved practical to investigate the interactions

of chlorofibers and the procedural variables pertaining to the DSC cell in greater detail since even the presence of a purge gas (100 ml min^{-1}) was insufficient to protect the cell from corrosion by gaseous products*. For this reason, even though the DSC cell is more convenient to use for fiber and fabric samples and gives improved thermoanalytical performance, the standard DTA cell (in the Du Pont system) is preferred for routine identification of unknown fibers by "fingerprint" thermograms.

In either case, it should be recognised that the cell itself can contribute substantially to the shape of the DTA curve obtained; in the case of the standard cell by retention of volatile products in the proximity of the sample, and in the case of the DSC cell by further interaction of the sample or products with the aluminium pan. Great caution is therefore required when measures of thermal/chemical stability are compared to other properties of interest such as strength retention or flame resistance.

The various fibers containing chlorine have characteristic DTA curves, which are in some cases sensitive to procedural variables. There can be no confidence that the DTA curves of any particular blend, mixture or alloy of two or more components will be additive in respect of decomposition, although greater reliance can be placed on first order transitions.

REFERENCES

1 R. F. Schwenker and P. J. Chatterjee, in R. C. Mackenzie (Ed.), *Differential Thermal Analysis*, Vol. 2, Academic Press, London, 1972, Ch. 41.
2 *Identification of Textile Materials*, The Textile Institute, Manchester, 6th ed., 1970.
3 R. F. Schwenker, in *Analytical Methods for a Textile Laboratory*, AATC Monograph No. 3, American Association of Textile Chemists and Colorists, 1968.
4 P. Dunn and B. C. Ennis, *Thermochim. Acta*, 3 (1971) 81.
5 J. S. Crighton and D. A. Holmes, in H. G. Wiedemann (Ed.), *Thermal Analysis*, Vol. 3, Birkhauser Verlag, Basle, 1972, p. 411.
6 S. M. Tarim and D. M. Cates, *Appl. Polym. Symp.*, 2 (1966) 1.
7 R. W. Michelson, *Thermochim. Acta*, 5 (1973) 329.
8 M. A. Bingham and B. J. Hill, *J. Therm. Anal.*, 7 (1975) 347.
9 P. Dunn and B. C. Ennis, *J. Appl. Polym. Sci.*, 14 (1970) 355.
10 *DTA Reference Thermograms: Polymers and Related Products*, Sadtler Research Laboratories Inc., Philadelphia, 1967.
11 R. A. Baxter, in R. F. Schwenker and P. D. Garn (Eds.), *Thermal Analysis*, Vol. 1, Academic Press, New York, 1969, p. 65.
12 J. G. Cook, *Handbook of Textile Fibres*, Merrow Publishing Co., Watford, 3rd ed., 1964, p. 334.
13 T. Koshiro and A. Goldfarb, *Mod. Text.*, 54 (1973) 40.
14 R. K. Kennedy, in H. F. Mark, S. M. Atlas and E. Cernia (Eds.) *Man Made Fibres: Science and Technology*, Vol. 3, Interscience, New York, 1968, p. 199.
15 J. G. Cook, *loc. cit.*, p. 627.
16 J. G. Cook, *loc. cit.*, p. 327; L. Gord, in H. F. Mark, S. M. Atlas and E. Cernia (Eds.), *loc. cit.*, p. 327.

* Contamination and corrosion of the cell can lead to baseline drift, excessive noise, reduced sensitivity, and spurious peaks. Reversible phenomena have been observed at times, for example an endothermic peak at 260°C, reversible at the *same temperature* on cooling. The constantan "Thermo-Electric Disc" in the DSC cell has a limited life, which is shortened if corrosive products are liberated from the sample.

17 A. P. Gray, in R. S. Porter and J. F. Johnson (Eds.), *Analytical Calorimetry*, Plenum Press, New York, 1968, p. 209.
18 D. Dollimore, L. F. Jones and T. Nicklin, *Thermochim. Acta*, 11 (1975) 307.
19 L. W. Collins and W. W. Wendlandt, *Thermochim. Acta*, 11 (1975) 253.
20 T. Osugi, in H. F. Mark, S. M. Atlas and E. Cernia (Eds.), *loc. cit.*, p. 245.
21 P. Dunn and B. C. Ennis, *J. Appl. Polym. Sci.*, 14 (1970) 1795.

Thermochimica Acta, 21 (1977) 59–88

A NEW METHOD FOR THE SIMULTANEOUS DETERMINATION OF THE SIZE AND THE SHAPE OF PORES: THE THERMOPOROMETRY

MAURICE BRUN, ANDRÉ LALLEMAND, JEAN-FRANÇOIS QUINSON AND CHARLES EYRAUD

Laboratoire de Chimie Appliquée et de Genie Chimique, Université de Lyon, E.R.A. au C.N.R.S., 300 Lyon (France)

(Received 8 December 1976)

ABSTRACT

A thermodynamic study of the liquid–solid phase transformations in porous materials provides the relationships between the size of the pores in which solidification takes place and the temperature of the triple point of the divided liquid, on the one hand, and between this temperature and the apparent solidification energy on the other hand.

The experimental study of the phase transformations, carried out by means of a microcalorimeter, gives the values of the parameters necessary to calculate the free solid–liquid interphase extension energy γ_{ls} at different temperatures. A formula $\gamma_{ls} = f(T)$ is given for water and benzene. Once this factor is known, it is possible to study the numerical relationship between pore-radius and freezing energy at the equilibrium temperature.

By using these relations together with the solidification thermogram (the recording of the power evolved by the solidification of a capillary condensate during a linear decrease of temperature) the authors have been able to determine pore distribution curves. An emphasis is put on the comparison between this method, thermoporometry, and the B.J.H. method.

Last of all the comparison of the experimental data for solidification and melting provide information concerning pore shape by means of the evaluation of a thermodynamic shape factor or by a method of simulation of porous material.

INTRODUCTION

The important role played by porous materials in industries dealing with oil, chemicals, paper-production, textiles, building, leather, ... etc. has promoted the research and the application of a number of techniques aimed at studying porosity. Dullien and Batra[1] have recently made a thorough and critical review of them. These techniques can be classed as:

(a) Direct observation methods using electronic microscopes and the diffraction

of X rays. Unfortunately, those techniques which make it possible to observe the structure of the material directly prove to be difficult to handle when it comes to examining mesoporous materials whose mean pore-radius ranges from 2 to 50 nm.

(b) Indirect methods based on the analysis of capillary phenomena occurring in porous materials. The most frequently used of these methods are mercury porosimetry for the larger pores and the B.J.H. method for the narrower ones. The latter deduces the characteristics of the porous material from the conditions of the liquid → gas transformation of a condensate held inside the material. Thus, it provides information about the size of the mouths of the pores.

The authors of this paper have recently presented a new technique of indirect study: thermoporometry, which analyses the conditions of the solid–liquid phase transformation of a condensate held inside the porous materials[2, 3].

This method is based on the observation, mentioned by several authors[4–6] that the conditions of equilibrium of the solid, liquid and gaseous phases of a pure substance which is highly dispersed are determined by the curvature of the interfaces. In the case of a liquid contained in a porous material the solid–liquid interface curvature depends closely on the size of the pore. The solidification temperature is therefore different in each pore of the material.

The solidification thermogram of a known condensate inside an unknown material thus leads to the deduction of: the size of the pores by means of the measurement of the solidification temperature, and the volume of these pores through the measurement of the energy involved in the phase transformation.

This method actually gives the real size of the pores and not that of their necks.

Until recently the method had only been used as a relative method using calibration curves drawn from well-known samples. It seemed to us worthwhile to turn it into an absolute method, enabling us to deduce the pore-size distribution from the solidification thermogram purely by means of theoretical relationships.

Besides, in a number of applications where porous materials are used as filtering elements, it seemed worthwhile to know the shape of the pores—a key component of their permeability.

Thermoporometry makes it possible, by comparing the melting and solidification thermograms, to deduce the shape of the pores and to present a model of material made up of cylindrical and spherical pores.

2. STUDY OF PORE-SIZE DISTRIBUTION

2.1. Principle of the method: Solidification of a liquid in a porous material

2.1.1. Relationship between the temperature of the triple point of a condensate and the radius of the pore

2.1.1.1. Solification temperature of a highly dispersed liquid. For a pure non-divided material the conditions of equilibrium of the three phases only coexist at the

T_0 triple point. There is only one such point. In the case of divided phases there is no longer just one point: the equilibrium pressure and temperature of the three phases are determined by the curvature of the menisci. The phase rule established by Defay then gives a variance of 2.

Indeed in a finely divided substance the surface energy can no longer be ignored. According to Gibbs' model we then have to admit that two phases i and j, whose volumes are V_i and V_j, are separated by a surface layer, the interphase ij, whose surface is A_{ij} and whose thickness can be ignored. The Gibbs–Duhem equations then are:

$$\begin{aligned} &S_i\,\mathrm{d}T - V_i\,\mathrm{d}P_i + m_i\,\mathrm{d}\mu_i = 0 \qquad \text{for the phases} \\ &S_{ij}\,\mathrm{d}T + A_{ij}\,\mathrm{d}\gamma_{ij} + m_{ij}\,\mathrm{d}\mu_{ij} = 0 \qquad \text{for the interphases} \end{aligned} \tag{1}$$

where T is the temperature, m the mass, S the entropy, μ the chemical potential and where the pressures P_i and P_j are related to the free surface extension energies γ_{ij} according to Laplace's equations:

$$P_j - P_i = \gamma_{ij}\frac{\mathrm{d}A_{ij}}{\mathrm{d}V_j}. \tag{2}$$

At the triple point the three phases of a pure substance are in equilibrium with their three interphases, so that the six chemical potentials are equal.

$$\begin{aligned} &\mu_i = \mu_j = \mu_{ij} = \mu_{jk} = \ldots \text{ and} \\ &\mathrm{d}\mu_i = \mathrm{d}\mu_j = \mathrm{d}\mu_{ij} = \mathrm{d}\mu_{jk} = \ldots \end{aligned} \tag{3}$$

By subtracting two by two the Gibbs–Duhem equations as applied respectively to the l (liquid), s (solid) and g (gaseous) phases, and by taking into account (2) and (3) we obtain

$$\left(\frac{s_s - s_g}{v_s - v_g} - \frac{s_l - s_s}{v_l - v_s}\right)\mathrm{d}T = \frac{v_g}{v_g - v_s}\,\mathrm{d}\left(\gamma_{sg}\frac{\mathrm{d}A_{sg}}{\mathrm{d}V_g}\right) - \frac{v_l}{v_l - v_s}\,\mathrm{d}\left(\gamma_{sl}\frac{\mathrm{d}A_{sl}}{\mathrm{d}V_l}\right) \tag{4}$$

where s and v stand for the specific entropy and volume of the substance.

This differential equation of the triple point temperature shows indeed that the temperature depends on the curvature of 2 interphases. It is obvious that two similar equations could be obtained by simply permuting systematically the s, l, g subscripts and that the three equations together will have covered all the possible combinations of interphases.

2.1.1.2. Relationship between the triple point temperature of a condensate which saturates a porous material and pore-radius. It appears from the previous study that in order to calculate the triple point temperature it is necessary and sufficient to know the $\mathrm{d}A_{ij}/\mathrm{d}V_j$ curvature of two of the three interphases. This condition can usually not be met for a porous material but it is possible to study the particular case where

the solid–gas interphase is plane. For this a quantity of condensate whose volume is slightly superior to that of the pores can be used. Below the normal T_0 triple point the excess solidifies and the interphase thus obtained remains flat at any temperature inferior to T_0. The dA_{sg}/dV_g curvature then is always zero. As $v_g \gg v_l$ and as $s_s - s_l = \Delta S_f$ is the solidification entropy of the condensate, eqn (4) becomes:

$$\Delta S_f \, dT + v_l \, d\left(\gamma_{ls} \frac{dA_{sl}}{dV_l}\right) = 0 \tag{5}$$

This equation therefore shows a unique correspondence between the triple point temperature and the curvature of the solid–liquid interphase. In order to relate the temperature to the pore size, it is then necessary to know to what extent the curvature is related to the pore-radius and, for that purpose, to study the solidification process of a liquid which is divided by a porous material.

(a) Solidification process by nucleation

In a homogeneous liquid, solidification occurs from critical nuclei. One should remember that embryos appear spontaneously in the liquid but that they cannot grow unless they reach a minimum size called critical size, whose value decreases with the temperature of the environment. In a porous material the embryo is not free to reach its critical size at any temperature as its mean radius will at most be equal to the radius of the cavity inside which it is. At the normal solidification temperature, the embryos therefore cannot reach the critical size in the pores. When the temperature of the saturated sample is lowered, solidification can occur progressively in the smaller pores (according to their size) when the size of the critical nuclei (at a given temperature) is the same as that of the pore.

(b) Solidification process by evaporation followed by sublimation

Some authors[7, 8] claim that solidification occurs through evaporation of the liquid followed by a condensation into solid state, both outside the porous material and inside the larger pores. Such a process can be understood in the case of a steep thermal gradient but is inconceivable when the phases are in equilibrium. Indeed it can be shown, with the help of eqn (5), that solidification would follow that process at a temperature inferior to nucleation temperature, the freezing temperature depressions[9] being in the ratio γ_{lg}/γ_{ls}.

Consequently such a process could only occur in the case of a strong thermodynamic imbalance, due for instance to a strong supercooling or to a temperature gradient. Last of all, when the porous material is thoroughly saturated, it must be admitted that the vapour phase does not exist in it, which prevents the process from occurring.

(c) Solidification process by progressive penetration of the solid phase

Everett submits another process consisting of a progressive penetration of the solid phase formed outside the porous material into the smaller, then the smallest

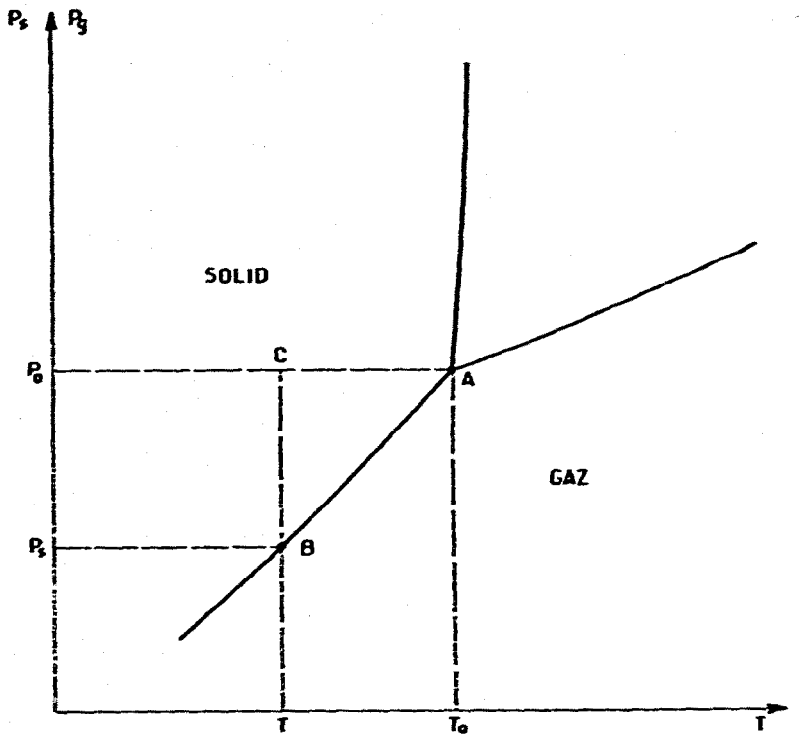

Fig. 1. Phase diagram.

pores[10]. That process which occurs at the same temperature for each size of the pores as nucleation most probably occurs jointly with the latter. But it cannot account by itself for the solidification which can be observed in an unsaturated material in which only the smaller pores are filled with condensate; neither does it apply to a material with ink-bottle shaped pores.

On noting that supercooling is unlikely for a highly divided fluid (as is the case in a porous material) it becomes possible to opt for the first-mentioned process. The curvature radius of the nucleus, i.e., of the solid–liquid interphase, equals then the R_p radius of the pore under study. Actually, as will be shown later in this paper, the molecules which are in close contact with the wall are not affected by the change of state. Thus the curvature radius of the solid–liquid interphase is R_n, the pore radius minus the thickness t of the layer of the molecules which are not affected by the solidification. Assuming the shape of the interphase to be that of a spherical cap, its curvature has the value:

$$\frac{dA_{sl}}{dV_l} = -\frac{2}{R_n}$$

By substituting this value into eqn (5) we obtain

$$\frac{1}{R_n} = \frac{1}{2\gamma_{ls}} \int_{T_0}^{T} \frac{\Delta S_f}{v_l} dT \qquad (6)$$

This equation makes it possible for each temperature T to determine the radius of the pores inside which the condensate solidifies.

2.1.2. *Solidification entropy of a capillary condensate*

2.1.2.1. Solidification entropy of a divided substance. On the diagram of the phases equilibrium (Fig. 1), it is possible to find a transformation similar to the solidification of a divided liquid and thus to evaluate in a simple way the variation of any state function, in particular entropy, when the above-mentioned solidification occurs.

In the case under study the solid–gas interphase is plane and the triple point moves along the normal solid–gas equilibrium curve. At a T temperature the triple point is in B and the solidification entropy ΔS_f is then equal to the normal solidification entropy ΔS_{fo} plus the entropy variation of the solid along the line ACB and also the entropy variation of the liquid along the equivalent line, but taken inversely, with respect to supercooled liquid phase. For that evaluation it must be noticed that the pressure P_l of the liquid phase in B is different from the pressure of the solid and gaseous phases P_s.

When c is the specific heat capacity at constant pressure and h the compression heat,

$$\Delta S_f = \Delta S_{fo} + \int_{P_l}^{P_o} \frac{h_l}{T}\,dP + \int_{T}^{T_o} \frac{c_l}{T}\,dT + \int_{T_o}^{T} \frac{c_s}{T}\,dT + \int_{P_o}^{P_s} \frac{h_s}{T}\,dP$$

Assuming the condensed phases to be incompressible and noting that

$$\frac{h}{T} = -\left(\frac{\partial v}{\partial T}\right)_P$$

$$\Delta S_f = \Delta S_{fo} + \int_{T_o}^{T} \frac{c_s - c_l}{T}\,dT + \left[\left(\frac{\partial v_l}{\partial T}\right)_P - \left(\frac{\partial v_s}{\partial T}\right)_P\right]_T (P_s - P_o)$$

$$+ \left[\left(\frac{\partial v_l}{\partial T}\right)_P\right](P_l - P_s) \qquad (7)$$

where P_s is the vapour pressure of the undivided solid at temperature T. Its value is given by Clapeyron's equation and $P_l - P_s$ is given by Laplace's equation.

$$P_s - P_l = \frac{2\gamma_{ls}}{R_m} = \int_{T_o}^{T} \frac{\Delta S_f}{v_l}\,dT \qquad (8)$$

2.1.2.2. Effect produced on the entropy of superficial phases by the change of state. Along with solidification there occurs a change of interphase between the layers

which do not freeze and the adjacent phase (liquid before solidification, solid afterwards). The additional entropy variation thus obtained can be evaluated by using the equations of Gibbs–Duhem (1) as applied to each of the interphases, the equality of chemical potentials (3) and Young's formula dealing with the equilibrium of the three interphases[3]:

$$(\Delta S_f)_{sup} \# - \frac{2v_l}{R_n} \frac{d\gamma_{ls}}{dT} \tag{9}$$

2.1.2.3. Solidification energy of a capillary condensate. The solidification entropy of a capillary condensate is therefore given by adding $(\Delta S_f)_{sup}$ to ΔS_f, and then the theoretical solidification energy is

$$W'_{th} = T[\Delta S_f + (\Delta S_f)_{sup}] \tag{10}$$

$$\text{or } W'_{th} \# T\Delta S_f \left[1 - \frac{d\gamma_{ls}}{dT} \frac{\Delta T}{\gamma_{ls}}\right] \tag{11}$$

However, as was mentioned above a layer with thickness t is not affected by the state change, so that in a pore with a V_p volume only the volume V'_p solidifies and the apparent energy of the state change in the pore under study (the only thing that can be measured) is

$$W_a = W'_{th} \cdot \frac{V'_p}{V_p} \tag{12}$$

At any temperature the knowledge of the energy evolved makes it possible to determine V_p.

2.2. Numerical evaluation of the various parameters

In order to be applied, the previous equations require the evaluation of several parameters whose numerical values do not appear in the literature as the liquids are usually supercooled in the case under study. It is therefore necessary to determine those values for the 2 condensates used in this investigation, water and benzene.

2.2.1. Solidification energy of the divided liquid

The literal formula of this energy is provided by eqn (7).

(a) In the case of water

By adopting the following values[11, 12] where θ is the temperature in °C.

$$c_s = 2.114\,(1 + 373.7\,\theta \cdot 10^{-5})\ J\ g^{-1}$$

$$c_l = 4.222\,(1 - 54 \cdot 10^{-5}\,\theta)\ J\ g^{-1}$$

$$\left(\frac{\partial v_l}{\partial T}\right)_P = -9.11 \cdot 10^{-5}(1 - 0.227\,\theta)\ \text{cm}^3\,\text{g}^{-1}\,\text{K}^{-1}$$

$$\left(\frac{\partial v_s}{\partial T}\right)_P = 12.28 \cdot 10^{-5}\ \text{cm}^3\,\text{g}^{-1}\,\text{K}^{-1}$$

$$\Delta S_{f_o} = -1.2227\ \text{J}\,\text{g}^{-1}\,\text{K}^{-1}$$

$$P_o = 4.58\ \text{mm Hg}$$

$$v_l = 1.000132\,(1 - 9.10 \cdot 10^{-5}\,\theta + 1.035 \cdot 10^{-5}\,\theta^2)\ \text{cm}^3\,\text{g}^{-1}$$

eqn (7) becomes

$$\Delta S_f(\text{J}\,\text{g}^{-1}\,\text{K}^{-1}) = \underbrace{-1.2227}_{\text{A}} - \underbrace{\left[4.889\ \text{Ln}\frac{T}{T_o} - 10.18 \cdot 10^{-3}\,\theta\right]}_{\text{B}}$$

$$\underbrace{+\,9.11 \cdot 10^{-5}(1 - 0.227\,\theta)\int_{T_o}^{T}\frac{\Delta S_f}{v_l}\,dT}_{\text{C}}$$

In this formula term A represents the normal entropy, term B the entropy variation due to the lowering of the transformation temperature, term C the one due to the liquid–solid interphase curvature. The influence of the solid pressure is negligible here.

Term C is only a correcting term. Therefore, an approximation can be made which enables it to be integrated as follows:

$$\int_{T_o}^{T}\frac{\Delta S_f}{v_l}\,dT \# \frac{1}{v_l}\int_{T_o}^{T}\Delta S_f\,dT \simeq \frac{1}{2v_l}(\Delta S_f + \Delta S_{f_o})(T - T_o)$$

whence

$$\Delta S_f(\text{J}\,\text{g}^{-1}\,\text{K}^{-1}) = -1.2227 - 4.889\ \text{Ln}\frac{T}{T_o} + 10.18 \cdot 10^{-3}\,\theta$$

$$+\,4.556 \cdot 10^{-5}(\theta - 0.227\,\theta^2)(\Delta S_f + \Delta S_{f_o})$$

$$\Delta S_f(\text{J}\,\text{g}^{-1}\,\text{K}^{-1}) =$$

$$\frac{-1.2227 - 4.889\ \text{Ln}\,(1 + \theta/T_o) + 10.126 \cdot 10^{-3}\,\theta + 1.256 \cdot 10^{-5}\,\theta^2}{1 - 4.556 \cdot 10^{-5}(\theta - 0.227\,\theta^2)} \qquad (13)$$

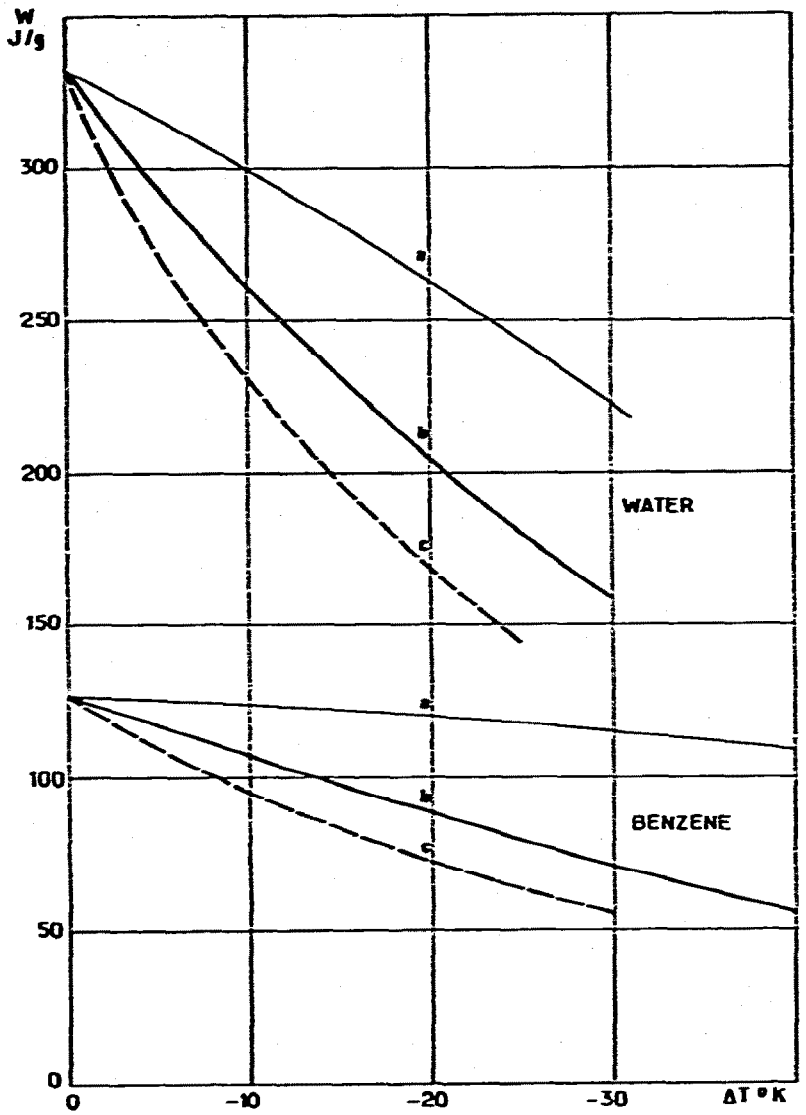

Fig. 2. Solidification energy of divided water and benzene (curves a). Apparent solidification energy (curves b) and apparent fusion energy (curves c) in porous materials.

With this equation, it is possible to determine the solidification energy of a divided liquid which is in equilibrium with the bulk solid, when the division does not take place in a porous material:

$$W_{th} = T\Delta S_f$$

Its variation is shown in Fig. 2. It can be seen that at − 30°C the solidification energy decreases by 108 J g^{-1}, i.e., 33%. The lowering of the transformation temperature has produced a variation of 72 J g^{-1}, and the lowering of the liquid pressure is responsible for a decrease of 36 J g^{-1}. There is no positive influence attributable to the lowering of solid and gaseous phase pressures.

The proposed formula is thus more precise than the one which is generally used, as the latter only takes into account the correcting term dealing with the temperature variation[13].

(b) In the case of benzene

By adopting the following values, which are valid in the area near the triple point

$\Delta S_{f_o} = -0.45687$ J g^{-1} K^{-1} (ref. 11) $T_0 = 278.7$ K

$v_l = 1.1108\,(1 + 1.184 \cdot 10^{-3}\,\theta)$ cm^3 g^{-1} according to Hu and Parsons[14]

$c_s = 1.60 + 9.50 \cdot 10^{-3}\,\theta + 3.75 \cdot 10^{-5}\,\theta^2$ according to Touloukian[15]

$c_l = 1.65 + 2.687 \cdot 10^{-3}\,\theta + 4.687 \cdot 10^{-6}\,\theta^2$ according to Touloukian[15]

eqn (7) becomes with $\Delta T = T - T_0$

$$\Delta S_f(\text{J g}^{-1}\text{ K}^{-1}) = \underbrace{-0.4568}_{\text{A}}$$

$$\underbrace{+\left[0.5373\ \text{Ln}\left(1 + \frac{\Delta T}{T_o}\right) + 1.641 \cdot 10^{-5}\,(T^2 - T_o^2) - 11.11 \cdot 10^{-3}\,\Delta T\right]}_{\text{B}}$$

$$\underbrace{-1.315 \cdot 10^{-3} \int_{T_o}^{T} \frac{\Delta S_f}{v_l}\,dT}_{\text{C}}$$

Terms A, B, C here represent the same variations as in the case of water. For the same reasons term C can be simplified, whence

$$\Delta S_f(\text{J g}^{-1}\text{ K}^{-1}) = -0.45687 - 11.11 \cdot 10^{-3}\,\Delta T + 1.641 \cdot 10^{-5}\,(T^2 - T_o^2)$$

$$+ 0.5373\ \text{Ln}\left(1 + \frac{\Delta T}{278.7}\right) - 0.592 \cdot 10^{-3}\,(\Delta S_f + \Delta S_{f_o})\,\Delta T$$

$$\Delta S_f(\text{J g}^{-1}\text{ K}^{-1}) =$$

$$\frac{-0.45687 - 10.84 \cdot 10^{-3}\,\Delta T + 1.641 \cdot 10^{-5}\,(T^2 - T_o^2) + 0.5373\ \text{Ln}\left(1 + \frac{\Delta T}{278.7}\right)}{1 + 0.592 \cdot 10^{-3}\,\Delta T} \qquad (14)$$

The solidification energy determined by means of this formula is shown in Fig. 2.

2.2.2. *Free extension energy of the liquid–solid interphase*

2.2.2.1. Values found in the literature. Several attempts have been made to measure the free extension energy of the liquid–solid interphases γ_{ls}. Most have proceeded by determining the limit temperatures of homogeneous nucleation and lead to rather erratic values. For water

$\gamma_{ls} = 23.8 \cdot 10^{-3} [1 \div 4.29 \cdot 10^{-3}\ \theta]$ N m^{-1} according to Dufour and Defay[16]

$\gamma_{ls} = 30.5 \cdot 10^{-3} [1 \div 9.3 \cdot 10^{-3}\ \theta]$ N m^{-1} according to Hesstvedt[17]

As for Skapski[18], he developed a procedure based on the relationship between the curvature of a solid held in a conical capillary and the temperature of its triple point, which leads to

$\gamma_{ls} = (44.5 \pm 10) \cdot 10^{-3}$ N m^{-1} for water and

$\gamma_{ls} = (21 \pm 7) \cdot 10^{-3}$ N m^{-1} for benzene

The discrepancies thus observed can be accounted for either by the unpredictability of supercooling, or by the approximations necessarily made when choosing a model for the application of the theory of homogeneous nucleation. In particular, no account is taken in this theory of the thickness of the transition layer between the liquid and solid phases. Yet, it can reach 30% of the radius of the critical nucleii at − 30°C. In the case of Skapski's experiments such approximations are much more acceptable as the thickness of the transition layer can be neglected as compared to the cone radius.

2.2.2.2. Experiment and results. It is possible to determine the value of γ_{ls} by applying eqn (6) to porous materials whose texture is known. By taking into account the previously determined value of ΔS_f this equation can indeed be integrated and written as

$$\frac{\gamma_{ls}}{R_n} + 2.09 \cdot 10^{-4}\,\Delta T = 0 \tag{15}$$

with $0 > \Delta T > -60$ for benzene

$$1.81 \cdot 10^{-4} \left(\frac{\gamma_{ls}}{R_n}\right)^2 + 1569\,\frac{\gamma_{ls}}{R_n} + \Delta T = 0 \tag{16}$$

with $0 > \Delta T > -40$ for water

where γ_{ls} is given in N m^{-1} and R_n in nm.

In order to determine γ_{ls}, it is therefore sufficient to measure the freezing point depression of condensates held in samples whose pore-radius R_p is known.

Because eqns (15) and (16) require the use of R_n, radius of the critical nucleus, it is necessary to determine the thickness t of the peripherical layer of the condensate which does not undergo a change of state. This thickness cannot be evaluated in the way Fagerlund[13] does, by comparing it to that of the adsorbed layer observed in the

process of an isothermal adsorption analysis. It is possible, however, to determine the thickness by measuring, in a calorimeter, the fraction of condensate which changes state in the cooling process. Such a calculation previously conducted by the authors of this paper[3] has enabled them to determine the number of molecular layers of benzene which do not solidify as 3.5, i.e., 13.3 Å and as 2.5, i.e., 8 Å for water. This result compares well with those obtained by Antoniou[19] who found less than three layers for water and by Litvan[20] who found two layers. We will therefore adopt a value of 13.3 Å for t in the case of benzene and 8 Å in the case of water, assuming these values to be practically independent of the pore size.

A calorimeter was used to measure the lowering of freezing temperature on a number of samples selected in view of the limited range of their pore-radii, made of eight alumina porous plugs with different mean pore radii and of Vycor glass. This last element makes it possible to prove that the nature of the material has practically no influence on the measurement.

The curves showing the distribution of pore radii were plotted by using the B.J.H. method and mercury porosimetry. The ΔT_M temperature depression given by the peak of the thermogram corresponds to freezing in the pores for which $W_a \cdot R_p^2 \, \Delta V/\Delta R_p$ is at its maximum[3]; hence, in the case of a sample with a limited range of pore radii, this temperature corresponds to the peak of the distribution curve. The results are shown in Table 1 for water and Table 2 for benzene.

TABLE 1

	Vycor	*Al*$_1$	*Al*$_2$	*Al*$_3$	*Al*$_4$	*Al*$_5$
$10^{10}\ R_p$ (m)	24	32	34	50	95	105
$10^{10}\ R_n$ (m)	14.5	22.4	24.4	40.4	83.5	95.4
ΔT_M (K)	28	28	21	15	7	7.1
$10^3\ \gamma_{ls}$ (N m^{-1})	21.9	34	28.8	35	34.7	40

TABLE 2

	Vycor	*Al*$_1$	*Al*$_2$	*Al*$_3$	*Al*$_6$	*Al*$_7$	*Al*$_8$
$10^{10}\ R_p$ (m)	24	32	34	50	55	99	135
$10^{10}\ R_n$ (m)	11	19	23	37	42	86	122
ΔT_M (K)	62	57	38	31.5	27	13.2	10.5
$10^3\ \gamma_{ls}$ (N m^{-1})	14.2	22.6	17.7	24.4	23.7	23.8	26.8

The values thus obtained for γ_{ls} do seem to be slightly inconsistent at times mainly because there was some uncertainty with respect to the pore size.

Assuming γ_{ls} to vary linearly with temperature, it is possible to determine the equation of the regression line by using the method of least squares

$$\gamma_{ls} = (40.9 + 0.39\,\Delta T)\,10^{-3} \tag{17}$$

with $0 > \Delta T > -40$ for water

$$\gamma_{ls} = (27.5 + 0.16\,\Delta T)\,10^{-3} \tag{18}$$

with $0 > \Delta T > -60$ for benzene

where γ_{ls} is given in N m^{-1}.

For $\Delta T \neq 0$ these equations give results in agreement with those given by Skapski, an allowance being made for the margin of error which he predicted. It can be noticed that in the -30, -40°C temperature range our value in the case of water is slightly higher than the one found for the same temperatures by using procedures based on the study of supercooling, probably for the reasons already mentioned.

2.2.3. Numerical relation between pore radius and triple point temperature

On substituting the value of γ_{ls} in eqns (15) and (16), it is possible to obtain the relationships between the freezing temperature depressions of a capillary condensate saturating a porous material and the radii R_g, and to deduce from this the variation curves $\Delta T = f(R_p)$ (Fig. 3). These curves can be represented by the following equations where R_p is given in nm.

$$R_p = -\frac{64.67}{\Delta T} + 0.57 \tag{19}$$

for water with $0 > \Delta T > -40$

$$R_p = -\frac{131.6}{\Delta T} + 0.54 \tag{20}$$

for benzene with $0 > \Delta T > -60$

It will be observed that:

(1) If the sample is not saturated the solid–gas interphases are not plane and according to eqn (4) the freezing point depression will be more marked than those calculated according to eqns (19) and (20).

(2) The two equations above are only valid when the condensate solidifies. In fact when fusion occurs in cylindrical pores the liquid–solid meniscus has a different shape from that of a critical nucleus, as will be seen below.

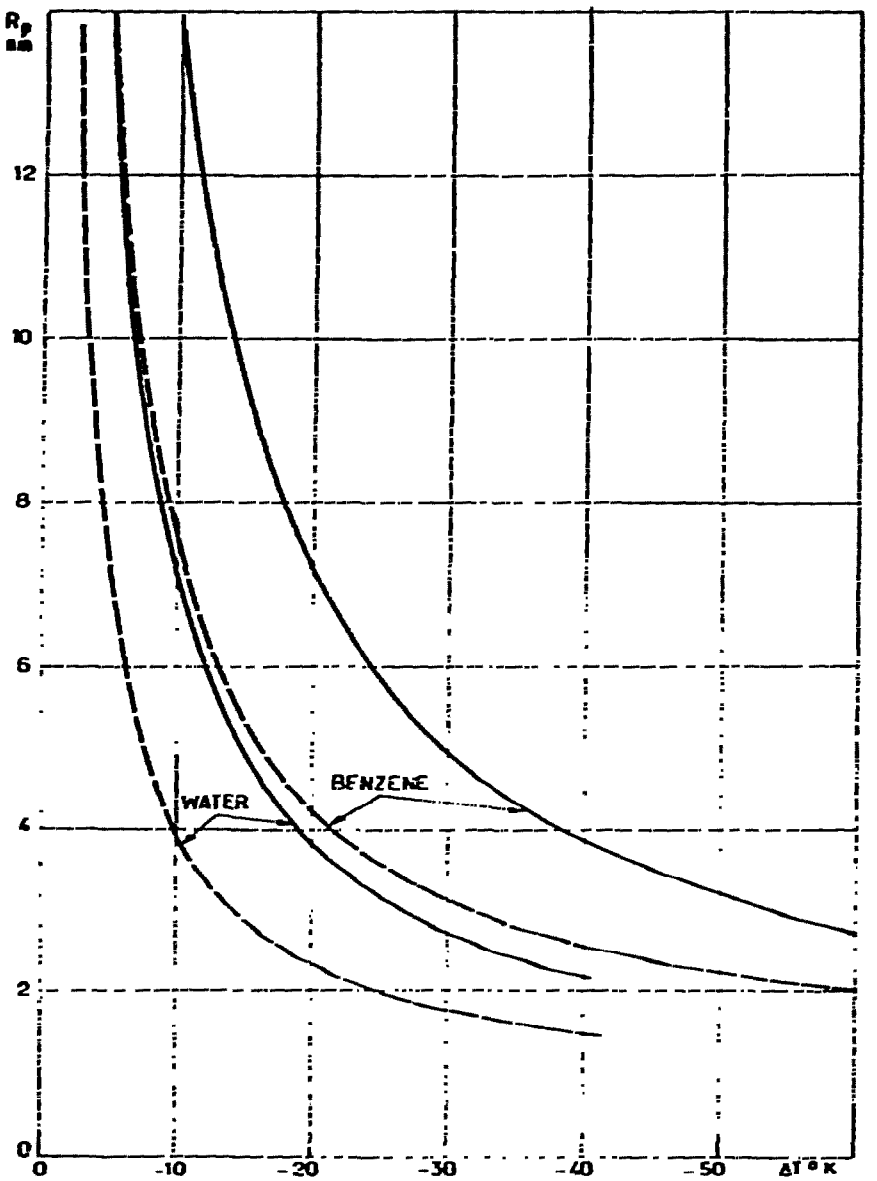

Fig. 3. Triple point temperature depression in porous materials at solidification (continuous lines) and at fusion (dashed lines).

2.2.4. Numerical relation between the apparent solidification energy of a capillary condensate and the temperature of the triple point

By substituting the values of $d\gamma_{lv}/dT$ and of R_n in eqn (9), it is possible to determine the entropy variation (ΔS_f) due to the transformation of the interphase: liquid-layers which do not undergo phase transformation into an interphase: solid-layers which do not undergo phase transformation.

$(\Delta S_f)_{sup} = -0.78/R_n$ for water
$(\Delta S_f)_{sup} = -0.36/R_n$ for benzene
where $(\Delta S_f)_{sup}$ is in J g^{-1} K^{-1}, R_n in nm.

For water contained in pores in which solidification occurs at -25°C, this correcting term represents a 25% increase of $|W_{th}|$.

In capillaries of any length L, the apparent solidification energy is then

$$W_a = W'_{th}\frac{\pi R_n^2 L}{\pi R_p^2 L} = W'_{th}\frac{[R_p - t]^2}{R_p}$$

Numerically and within the temperature range $0 > T > -40$°C this relation can be expressed by a quadratic equation

$$W_a = -5.56 \cdot 10^{-2}\,\Delta T^2 - 7.43\,\Delta T - 332 \text{ for water} \quad (21)$$
$$W_a = -8.87 \cdot 10^{-3}\,\Delta T^2 - 1.76\,\Delta T - 127 \text{ for benzene} \quad (22)$$

where W_a is expressed in J g^{-1}. The variation curves of W_a in terms of temperature are shown in Fig. 2.

2.3. Calorimetric determination of a pore radius distribution

As Bakaev et al.[21] and Antoniou[19] had hinted, it is possible to draw the curve of pore radius distribution of an unknown sample by analysing the solidification of a condensate held in the sample during the cooling process. Such a process has already been followed by the authors of this paper[22, 3] and Fagerlund[13]. This is an account of the procedure, using the results demonstrated above which deal with the relationship between pore radius, triple point temperature and solidification energy.

2.3.1. Principles of the procedure

At any temperature, freezing occurs in the pores whose sizes are given by eqns (19) or (20). The volume of these pores can be determined, in terms of the apparent solidification energy given by eqns (21) or (22), by a calorimetric measurement of the energy evolved at that temperature. The distribution curve is therefore directly deduced from the solidification thermogram.

2.3.2. Experimental procedure

To begin with, one to three grammes of the sample are degassed under vacuum, then they are thoroughly saturated with condensate by means of an evaporator. Both water and benzene are convenient here. However, in the case when a low porosity sample is under study, water has the advantage of having a high apparent solidification energy whereas in the case of samples with large pore radii benzene undergoes larger decreases of the triple point temperature.

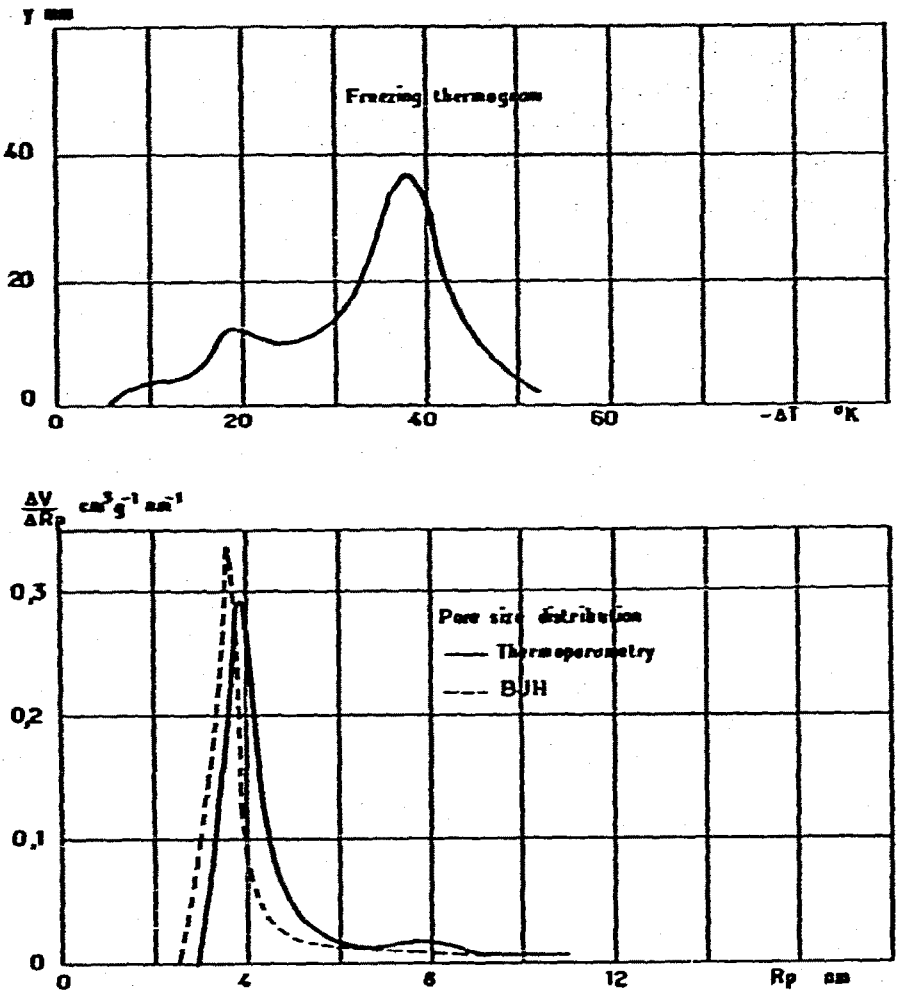

Fig. 4. Thermoporometry of a porous plug formed by compression of two powders.

The sample is then sealed and put into a calorimeter of the isothermal type built in the laboratory. The solidification thermogram is drawn during a linear lowering of temperature. The cooling speed is low enough (1 to 6 K h^{-1}) for the three phases to remain in constant equilibrium and the temperature to be the same throughout the sample.

The ordinate y of that thermogram corresponds to the deviation, expressed in mm, of the recorder under the influence of the power evolved. The abscissa, which is directly proportional to the time t, is also directly proportional to the temperature according to the equation:

$$\Delta T = k_1 t + k_2$$

The thermogram $y = f(\Delta T)$ shows a first peak which is characterized by a variant ΔT (within the range of a few degrees) due to the supercooling of the excess

of condensate. This peak does not appear in the figures here. Solidification inside the pores produces the part of the thermogram similar to that shown in Fig. 4, from which the distribution curve $\Delta V/\Delta R_p = f(R_p)$ can be deduced.

During the time interval dt, the energy which is evolved is proportional to the area $y\, d(\Delta T)$. The volume dV of the pores in which the change of state then occurs is directly proportional to the energy and inversely proportional to the apparent energy W_a; it is expressed by:

$$dV = k_3 \frac{y}{W_a} d(\Delta T)$$

The radius R_p being related to temperature T by an equation of the type

$$R_p = -\frac{A}{\Delta T} + B$$

its differential is

$$dR_p = -\frac{A}{(\Delta T)^2} d(\Delta T)$$

Therefore, the equation of the distribution curve is

$$\frac{\Delta V}{\Delta R_p} = k \frac{(\Delta T)^2}{W_a} y \tag{23}$$

where k is a factor taking into account the sensitivity of the calorimeter and the recorder, the rate of the temperature variation and of the recording as well as the slope A of the curve $R_p = f(1/\Delta T)$ and the mass of the sample under study.

This procedure has been satisfactorily applied to a large number of samples. As an example the results of the analysis of a double distribution sample will be given below.

2.3.3. Example of application

According to the theories which were tested to account for the change of state inside porous materials, thermoporometry should give the actual size of the cavities and not that of the necks, as is the case for the B.J.H. method.

In order to test that theory the sample under study was made up by mixing and compressing together 0.44 g of a powder A whose pores have a mean radius of 6 nm and 4.4 g of a powder B whose pores have a mean radius of 4 nm, the radii being measured by the B.J.H. method.

The solidification thermogram of the benzene contained in that sample and the distribution curve deduced from eqn (23), together with a distribution curve calculated by means of the B.J.H. method are shown in Fig. 4. It will be noticed that:

(a) The peaks of powder B nearly correspond, which substantiates the principle

of thermoporometry and the different equations required for its application.

(b) Thermoporometry brings to light a double distribution, already clearly visible on the thermogram, whereas the B.J.H. method shows only the peak due to the smaller pores. This supports the author's hypothesis about the solidification process. Indeed, if the very small proportion of powder A is taken into account, it can be assumed that it is brought in contact with the exterior only through the pores of powder B. That is why in this case the B.J.H. method only provides accurate information regarding the smaller pores which constitute the orifices of the mixture.

(c) The value of the radii thus obtained through thermoporometry in the case of powder B is slightly superior to that given by the B.J.H. method. This seems to point to the fact that the powder has orifices which are smaller than its cavities.

3. ANALYSIS OF THE PORE SHAPE

If information about the size of the pores is of capital importance to characterize a porous material, the knowledge of their shape is also valuable. Although the structure of most porous samples is a complex one, several authors have tried to compare them with models which would be as simple as possible. Three models of porous aggregates are usually suggested: an aggregate of cylindrical capillaries packed in series and in parallel[23], a porous material made up of tightly packed spheres[24] or a material with conical pores[25]. A critical survey and classification of the different models with which porous materials can be compared have been made by Karnaukhov[26]. From now on the material used in this paper will be assumed to be made up of both spherical and cylindrical pores.

3.1. Principle of the procedure

As was seen before, the solid phase in a pore only takes place from a spherical nucleus whose curvature is equal to twice the inverse of the radius; the freezing temperature depends on the radius according to the theoretical formula (6) and the numerical formulas (19) and (20).

With respect to fusion, the process is more complicated: If the pore is spherical, the curvature of the resulting solid condensate remains the same when fusion takes place as it was when solidification took place, and the fusion and solidification temperatures are the same. If the pore is cylindrical the spherical nucleus grows spontaneously and adopts the shape of the pore; the curvature of the solid condensate then becomes equal to the inverse of the radius. The relation between the radius and the temperature can be written as:

$$\frac{\gamma_{ls}}{R_n} = \int \frac{\Delta S_f}{v_l} \mathrm{d}T \tag{24}$$

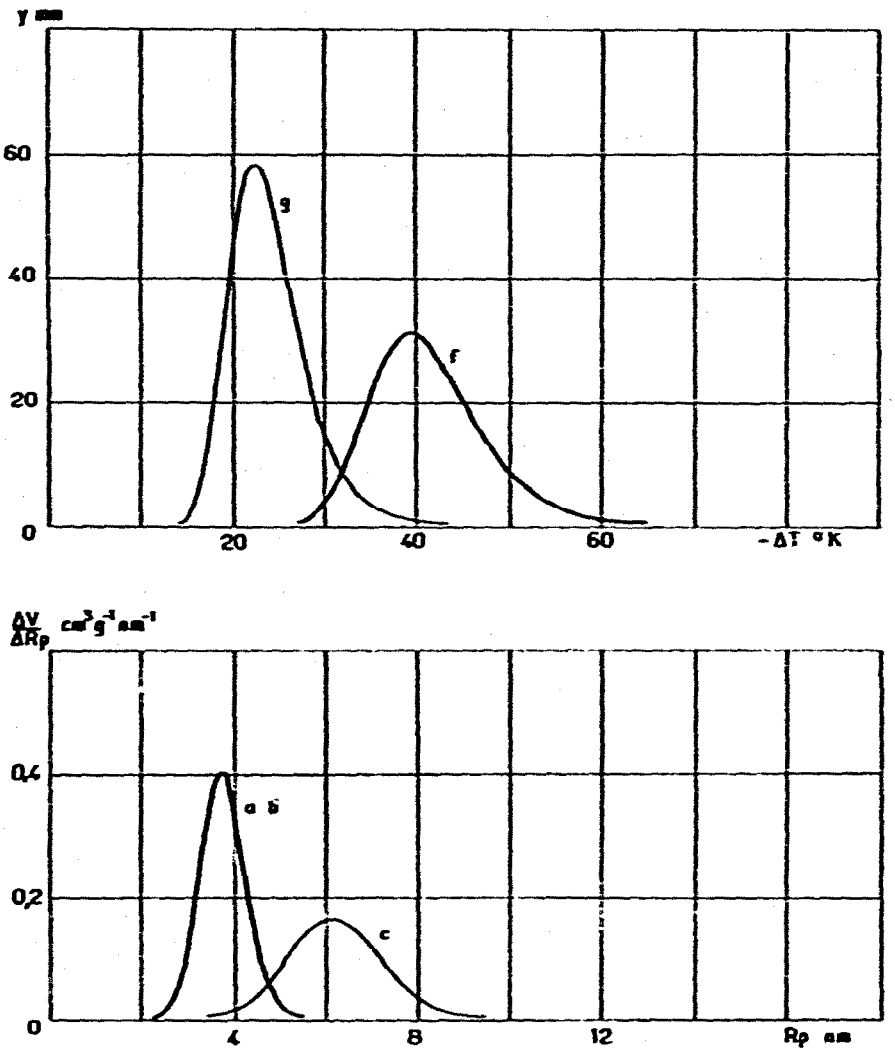

Fig. 5. Simulation of γ-alumina by cylindrical pores materials.

If in the case of freezing, the relation between R_n and the temperature depression ΔT is simply written as

$$R_n = f(\Delta T_f) \tag{25}$$

when fusion takes place it will be

$$R_n = \frac{1}{2} f(\Delta T_m) \tag{26}$$

The function f being the same in both cases.

These two equations bring to light the existence of a hysteresis between the freezing and fusion thermograms, when the pores are not strictly spherical.

The previous results point out that there is no ambiguity as far as the calculation

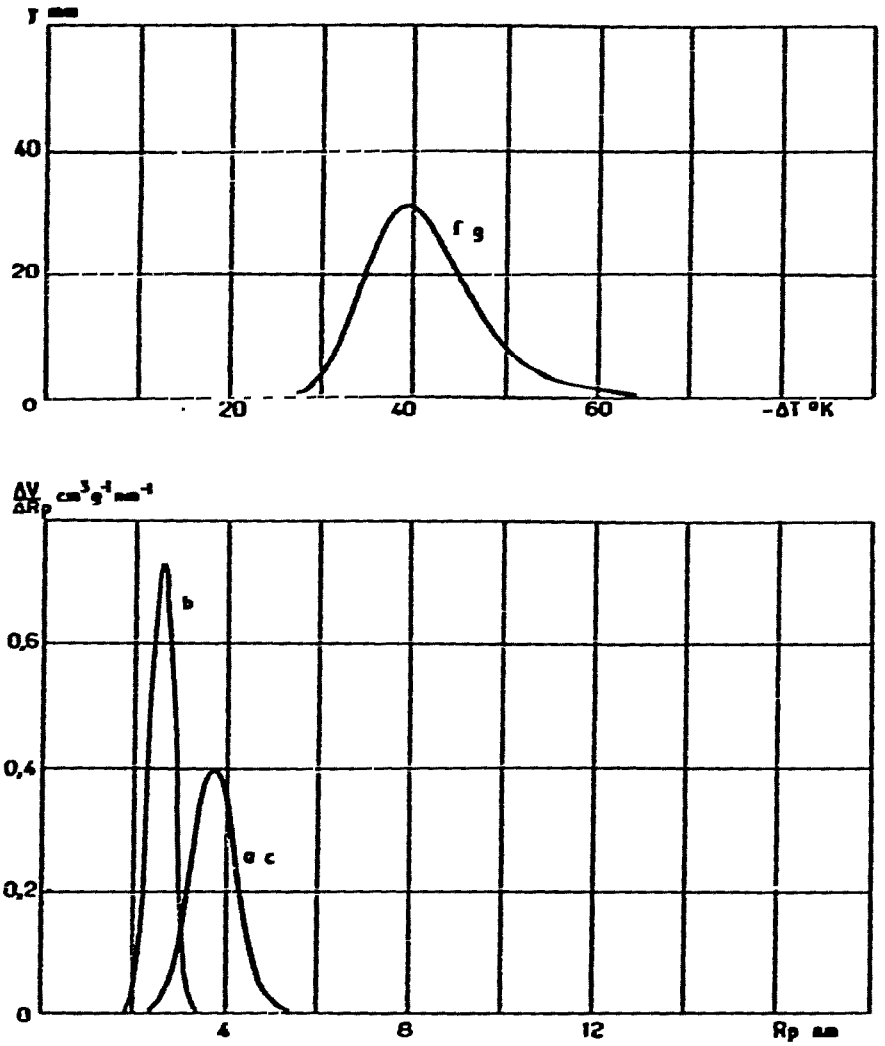

Fig. 6. Simulation of γ-alumina by spherical pores materials.

of the pore radius distribution curve, $\Delta V/\Delta R_p = f(R_p)$, is concerned in view of the freezing thermogram, whereas it would be necessary to know in advance the shape of the pores in order to deduce a distribution from the fusion thermogram. The latter then does not make it possible to obtain a distribution curve but it can still be used to provide information as to the shape of the pores.

Indeed, on assuming the pores to be first cylindrical and then spherical, two pore radius distribution curves can be drawn from this thermogram (Figs. 5 and 6), one called "spherical" (curve c) and the other "cylindrical" (curve b). The calculation of these two types of distribution must be conducted as shown in 2.3.2. It must be noticed, however, that if the relations between radius and temperature on the one hand, the apparent change of state energy and the temperature on the other hand, are the same as during solidification for "spherical" distribution, this is no longer the

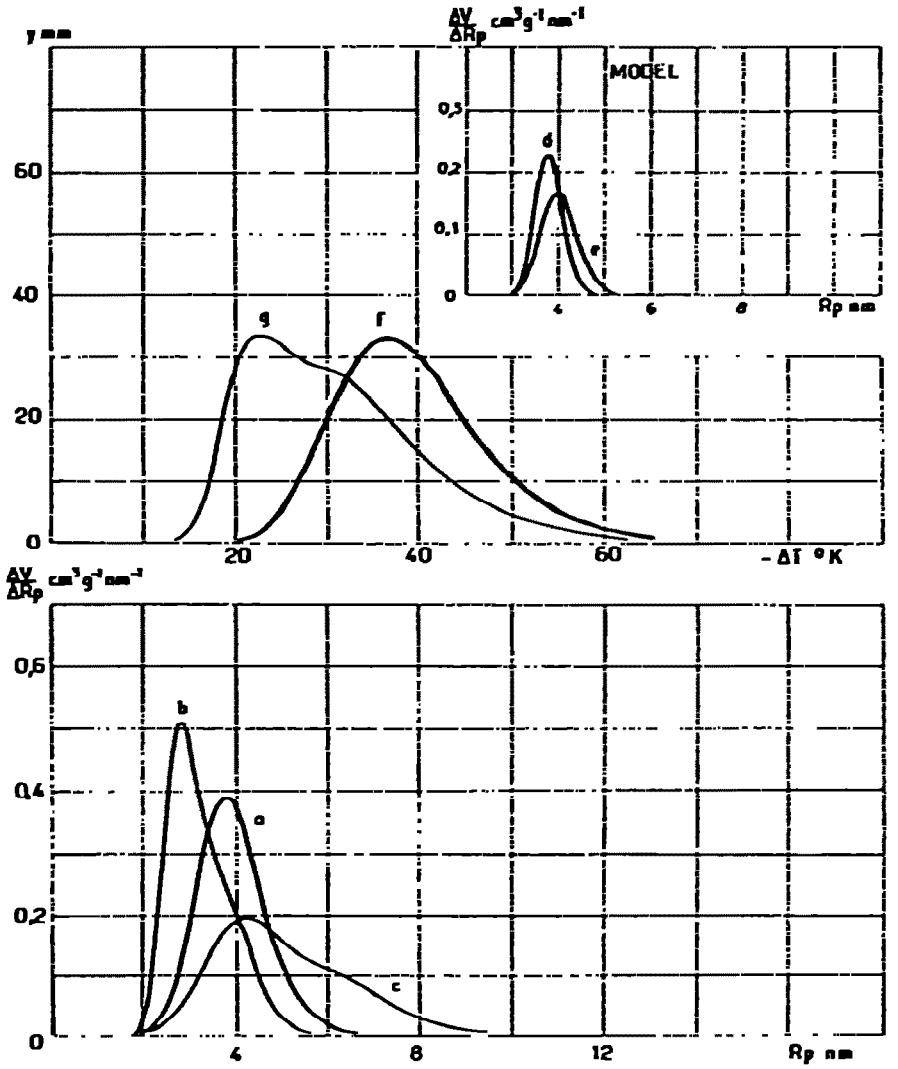

Fig. 7. Simulation of γ-alumina by cylindrical and spherical pores materials.

case for "cylindrical" distribution. In this last case the equation linking the apparent energy W_a to the temperature of the triple point is peculiar to fusion. In fact, whereas in the formula of W'_{th}, the variation W_{th} due to ΔS_f is a function of the temperature, the term $\Delta S_{f\,sup}$ is a function of the radius R_n whose relationship with temperature depends on the nature of the change of state—solidification or melting (eqn (6) or (24)). This should also be taken into account when the apparent energy is calculated according to eqn (12). Then the variation of W_a with respect to temperature, for the melting of a solid dispersed in a porous sample, shown in Fig. 2, appears as:

$$W_a = -0.155\,\Delta T^2 - 11.39\,\Delta T - 332 \quad \text{for water}$$
$$W_a = -0.0273\,\Delta T^2 - 2.94\,\Delta T - 127.3 \quad \text{for benzene} \qquad (27)$$

where W_a is expressed in J g^{-1}.

As was the case for solidification, these equations are only approximate, valid within the limits of these experimental investigations

$0 > \Delta T > -25$ for water and
$0 > \Delta T > -30$ for benzene.

Comparison between the hypothetical distribution curves (b) and (c) and the distribution curves deduced from the solidification thermogram (curve a) points to three possibilities:

(i) If (b) is strictly similar to (a), all the pores are cylindrical; the hysteresis of the thermograms (curves (f) and (g)) is then maximum (Fig. 5).

(ii) If (c) is similar to (a), all the pores are spherical and the solidification and melting thermograms correspond exactly (Fig. 6).

(iii) Usually as the pores are neither strictly spherical nor strictly cylindrical, curve (a) is situated between curves (b) and (c) (Fig. 7).

In order to improve the accuracy of the information about the shape of the pores provided by this kind of comparative study, two experimental procedures can be recommended: determination of a shape-factor and development of a model imitating the porous material.

3.2. Thermodynamic shape factor

By using the melting thermogram the hypothetical distribution curve c is drawn, assuming the pores to be spherical; for a given temperature the calculated radius R_c is given by eqn (25). As was mentioned before two extreme cases have to be considered: If the pores are actually spherical the ratio of radius R_c to the actual radius is one; and if the pores are cylindrical, radius R_c will be twice the actual radius, R the ratio R_c/R is 2. The ratio R_c/R which varies from 1 to 2 according to whether the pores are spherical or cylindrical, can be considered as a shape factor.

The above study deals with the nucleus radius R_n, and not with the pore radius R_p. Because distribution is related to pore radius, the previous deductions should be altered as follows:

As has been noted before, the equations relating pore radius to temperature in the case of spherical pores is of the type

$$R_p = \frac{A}{\Delta T} + B \tag{28}$$

Then, when melting occurs, the relationship between ΔT and the radius of cylindrical pores, obtained by taking into account equations 25 and 26, and the thickness t of the layers which do not change state, becomes

$$R_p = \frac{A}{2\Delta T} + \frac{B + t}{2} \tag{29}$$

or in numerical terms (Fig. 3)

$$R_p = -\frac{32.33}{\Delta T} + 0.68 \qquad \text{for water with } 0 > \Delta T > -40$$

$$R_p = -\frac{65.8}{\Delta T} + 0.92 \qquad \text{for benzene with } 0 > \Delta T > -60 \tag{30}$$

where R_p is expressed in nm and ΔT in K.

It can then be observed that if a hypothetical "spherical" distribution curve is drawn, for cylindrical pores, the relationship between pore radius R_{pc} given by eqn (28) and the real R_p given by eqn (29) will be

$$\frac{R_{pc}}{R_p} = 2 - \frac{t}{R_p}$$

The shape factor R_{pc}/R_p is therefore equal to 1 for spherical pores and to $2 - (t/R_p)$ for cylindrical pores. In the case of pores that are neither cylindrical nor spherical

$$1 < \frac{R_{pc}}{R_p} < 2 - \frac{t}{R_p}$$

It is worthwhile to alter the formula for the shape factor here so that the limit values of the factor may be independent of the radius. A thermodynamic shape factor is then defined by the formula

$$f_t = 1 - \frac{1 - \dfrac{R_{pc}}{R_p}}{1 - \dfrac{t}{R_p}} \tag{31}$$

This is equal to 1 for spherical pores and to 2 for cylindrical pores.

In practice, it was assumed that the porous material should be given the shape factor calculated for the pore radius corresponding to a 50% rate of liquid $\rightleftarrows$ solid transformation, measured from the cumulative volume curve

$$\Sigma \Delta V_p = f(R_p)$$

3.3. Development of a model simulating porous material

Although the shape factor gives information simply and quickly as regards the porous material texture, it is worthwhile to go on researching the subject and to build a model similar to the porous material. This research was done by means of a Hewlett-Packard 90-10 calculator.

The selected model is based on a porous structure made up of tightly packed cylindrical and spherical pores, characterized by the two corresponding pore radii distribution curves (Fig. 7, curves (d) and (e)). The formula for these distribution

curves was chosen to have a shape similar to the one obtained from experiments for most mono-distributed samples. It can be written:

$$\frac{\Delta V}{\Delta R_p} = (a\, R_p^2\, e^{-b\, R_p^2})^m$$

and it leads to a distribution curve starting from the origin at one end and leading to zero for the higher values of R_p at the other end. The existence of three parameters makes it possible to choose the maximum coordinates and the width of the distribution curve at 10% of its maximu' : amplitude.

Taking the "spherical" and "cylindrical" distributions as a starting point, the following curves can be calculated:

(1) The overall distribution curve (a) made up of curves (d) and (e).

(2) By means of the curve thus obtained, the solidification thermogram (curve f) drawn by using eqn (6) (numerical expressions (19) or (20)) in order to calculate ΔT for a given radius, and eqn (23) to determine the ordinate y.

(3) The melting thermogram (curve (g)) for which a distinction should be made between spherical and cylindrical pores. The way in which each of these two groups of pores contribute to the amplitude of the thermogram at a given temperature is obtained as follows:

– contribution of the spherical pores: the calculation is made by using the spherical pore distribution curve (curve (e)) as was done before for the solidification thermogram.

– contribution of the cylindrical pores: the same process as above is used, but curve (d) must be used as distribution curve; eqn (6) must be replaced by eqn (24) (numerical formula (30)) and in eqn (23) the energy evolved during solidification must be replaced by that evolved during melting (eqn (27)).

(4) The hypothetical "spherical" distribution curve (c) calculated from the fusion thermogram as was shown in paragraph 3.1. It is to be noted that it is not necessary to link to it the "cylindrical" distribution curve as the two imagined distribution curves are directly linked.

The different graphs obtained in this way are then compared to those obtained from experiments. It may then be necessary to alter the selected distributions (which were selected a priori) until the best possible agreement is obtained. Although a perfect agreement is never reached, the procedure based on simulation provides more complete information as regards texture than the one based on the shape factor. In order to illustrate the procedure, Fig. 7 shows the results achieved by assuming the structure of an γ-alumina, the experimental thermoporometric analysis of which is shown by the continuous line in Fig. 8. The corresponding curves are in good agreement. They can agree even better, however, as is pointed out by the model shown in Fig. 8, carried out by adding another spherical distribution to the selected model.

This example shows that the assumption of a porous material by the association of two types of pores gives good results, whereas the hypothesis of a porous material

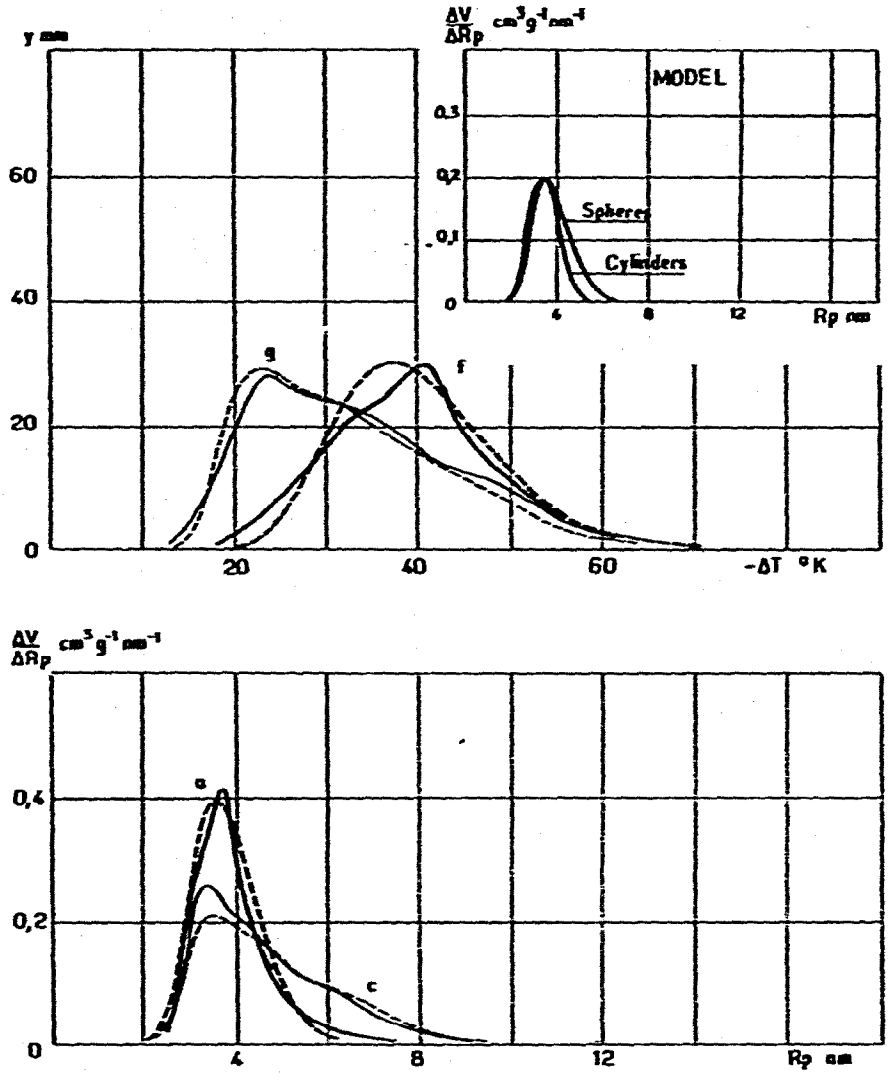

Fig. 8. Thermoporometry and simulation of non sintered γ-alumina. Continuous line, experimental curves; dashed line, simulation.

with only cylindrical pores or only spherical pores would provide a small degree of agreement, as is shown respectively in each case of simulation for γ-alumina in Figs. 5 and 6.

3.4. Application to the study of sintering

It seemed worthwhile to apply the two methods of investigation discussed above to a study of the influence of sintering on the pore shape of two mesoporous materials: γ-alumina and nickel fluoride, consolidated by the compression of their powder. In each case a benzene thermoporometry was carried out on untreated samples first, then on the same but sintered at different temperatures. The results

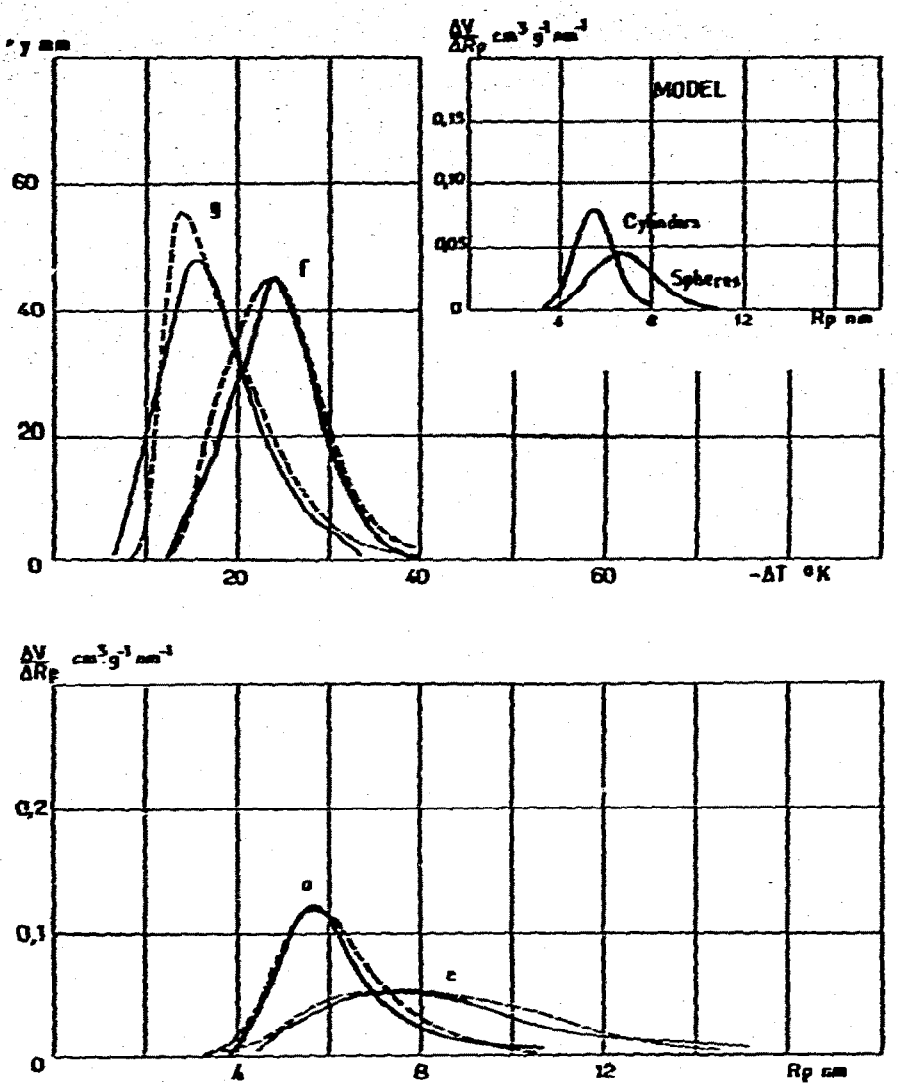

Fig. 9. Thermoporometry and simulation of sintered γ-alumina. Continuous line, experimental curves; dashed line, simulation.

TABLE 3

Material	T_s *(K)*	$R_{p\,o.s}$ *(nm)*	f_t
Alumina γ	—	3.7	1.25
	1250	6	1.51
Nickel fluoride	—	5.7	1.82
	850	10	1.94

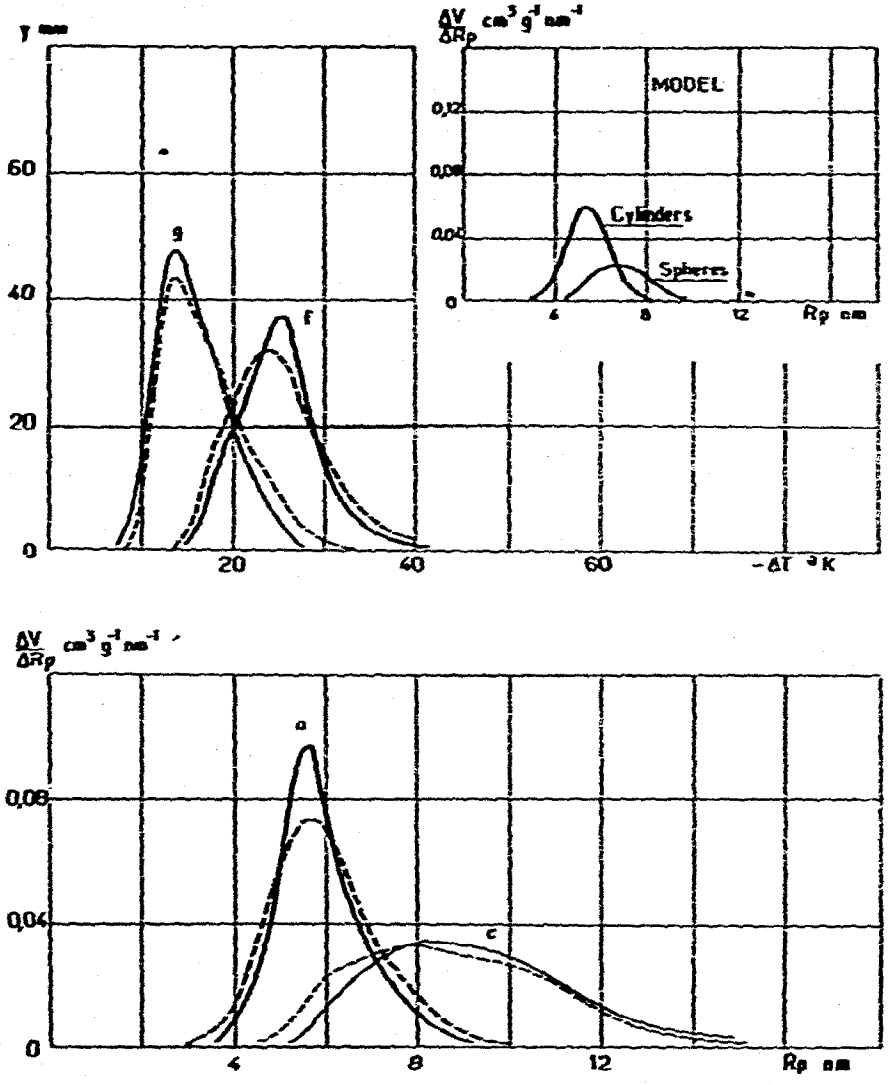

Fig. 10. Thermoporometry and simulation of non sintered NiF_2. Continuous line, experimental curves, dashed line, simulation.

relating to the extreme stages (untreated material, and material sintered at maximum temperature) are dealt with:

In Table 3 which gives the temperature T_s of sintering, the pore radius $R_{p\ 0.5}$ corresponding to a 50% rate of transformation and the thermodynamic shape factor connected with this radius.

In Figs. 8–11 where the thermograms and the distributions deduced from experiments and simulations are represented.

For both types of materials, it appears that sintering involves a widening of the pore size and a change in their shape towards the cylindrical form.

This last observation can be deduced from the increase of the shape factor as well as from the simulations. Indeed, in the selected models, an increase in the pro-

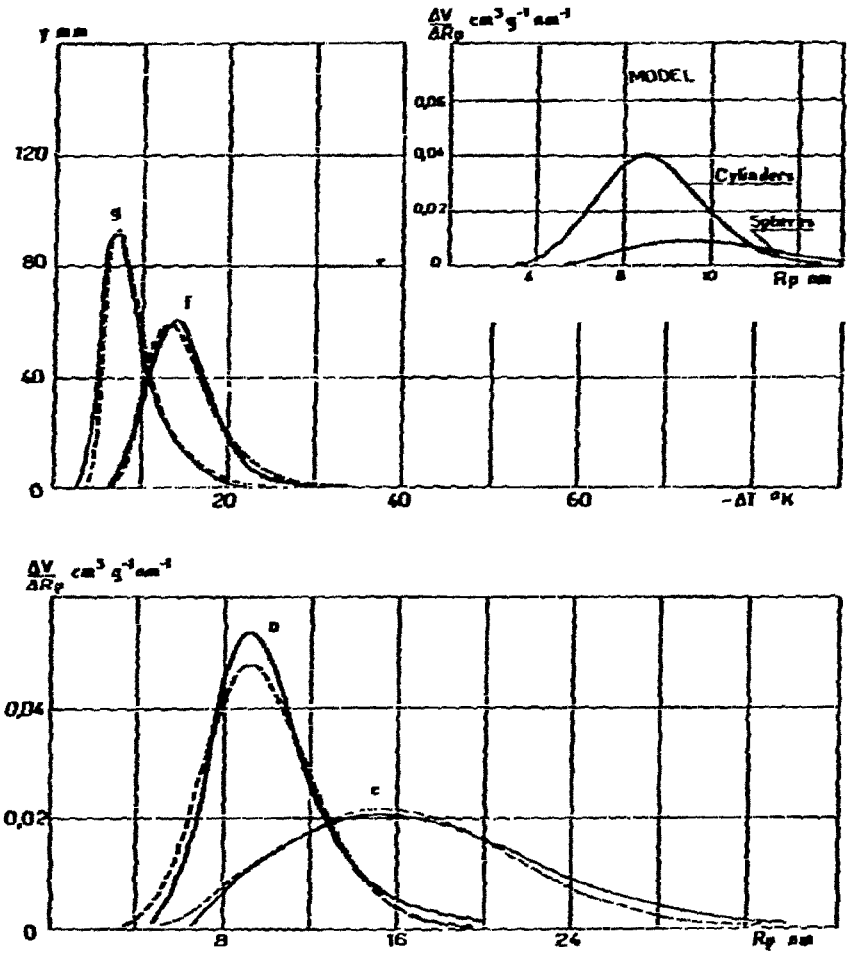

Fig. 11. Thermoporometry and simulation of sintered NiF_2. Continuous line, experimental curves; dashed line, simulation.

portion of cylindrical pores can be observed during the whole process of sintering.

The change is not so clear for nickel fluoride as for γ-alumina. This can be related to the fact that in the case of untreated materials a greater proportion of cylindrical pores can be observed to begin with in nickel fluoride as compared to γ-alumina.

CONCLUSION

The calorimetric procedure for determining the distribution of pore radii recommended until recently required the use of calibration curves $R_p(\Delta T)$ and $W_s(\Delta T)$ which differed with each condensate and were difficult to obtain. The

procedure described in this paper does away with calibration curves, due to the use of theoretical relationships. This is an undeniable improvement, as it is more accurate and makes it possible to use any condensate whose thermodynamic parameters c_p, v, ΔS_{fo} and γ_{ls} are known.

Because information concerning γ_{ls} is rare, a method of measuring it has been suggested. It was applied to water and benzene but, using the same porous materials, it could be applied more generally to any liquid able to condense. The accuracy of the results can be improved by a more accurate evaluation of the thickness of the layer which does not change state thanks to the use of other methods of investigation (R.M.N., adsorption calorimetry at low temperature, etc.).

The original purpose of thermoporometry—the determination of pore radius distribution curves—has been fulfilled again in the case of this new procedure, which is made clear by the comparison of its results with those of the B.J.H. method. Thermoporometry is simple to handle, it gives the real size of the cavities and it only requires a hypothesis about the pore shape when it comes to evaluating the volume of the layers which do not change state. All these advantages are definitely an improvement over the conventional methods.

The advantage goes even further in so far as it makes it possible to ascertain the pore shape of the material:

(i) The thermodynamic shape factor makes it possible to show to what extent the pore shape differs with the cylindrical model often propounded in the literature.

(ii) Simulation, as it is based on a porosity only consisting of spheres and cylinders, enables one to determine at the same time the radius and the volume of those two extreme types of pores. The development of a model of this type, by means of successive approximations, leads to a unique result whose agreement with the experimental results seems to be promising for the future of the method.

Thus thermoporometry appears as a method complete in itself which makes it possible to assess the porous material as a whole and to predict more accurately its behaviour in response to different thermal or mechanical treatments, together with its possible uses as ultrafilters, adsorbents, catalysts, etc.

REFERENCES

1 F. A. L. Dullien, and V. K. Batra, *Ind. Eng. Chem.*, 62 (1970) 25.
2 C. Eyraud, M. Brun, A. Lallemand, J. F. Quinson and L. Eyraud, *Pore Structure and Properties of Materials*, Vol. 1, Akademia, Prague, 1973, pp. C 81–99.
3 M. Brun, A. Lallemand, J. F. Quinson and C. Eyraud, *J. Chim. Phys.*, 6 (1973) 973.
4 P. Kubelka, *Z. Electrochem.*, 36 (1932) 611.
5 I. Higuti, *Sci. Rep. Tohoku Univ., Ser. I*, 33 (1940) 231.
6 R. Defay, I. Prigogine, A. Bellemans and D. H. Everett, *Surface Tension and Adsorption*, Longmans Green, London, 1966.
7 G. G. Litvan, *J. Colloid Interface Sci.*, 38 (1972) 75.
8 G. Berezkin, A. Kiselev and A. Kozlov, *J. colloid Interface Sci.*, 45 (1973) 190.
9 M. Brun, *Thèse*, Lyon, 1973.
10 D. Everett, *Trans. Faraday Soc.*, 57 (1961) 1441.
11 *Handbook of Chemistry and Physics*, 45e ed., The Chemical Rubber Co., Cleveland, Ohio, 1965.

12 *Am. Inst. of Phys. Handbook*, 2° Ed., Mac Graw Hill G., New York, 1963.
13 G. Fagerlund, *Mater. Constr.*, 6 (1973) 215.
14 P. M. Hu and R. W. Parsons, *Proc. Phys. Soc. London*, 72 (1958) 454.
15 Y. S. Touloukian, *Thermophysical Properties of Matter*, Vol. 6, IFI/Plenum, New York, 1970.
16 L. Dufour and R. Defay, *Thermodynamics of Clouds*, New York, London, 1963.
17 E. Hesstvedt, *Norv. Geotech. Inst. Pub.*, 56 (1964) 7.
18 A. Szapski, R. Billups and A. Rooney, *J. Chem. Phys.*, 26 (1957) 1350.
19 A. A. Antoniou, *J. Phys. Chem.*, 68 (1964) 10, 2754.
20 G. G. Litvan, *Can. J. Chem.*, 44 (1966) 2617.
21 V. A. Bakaev, V. F. Kiselev and K. G. Krasil'nikov, *Dokl. Akad. Nauk, SSSR*, 125 (1959) 831.
22 C. Eyraud, M. Brun, L. Eyraud, A. Lallemand and P. Eyraud, *C. R. Acad. Sci., Paris*, 273 B (1971) 645.
23 H. Adzumi, *Bull. Chem. Soc. Jap.*, 12 (1937) 199.
24 D. Dollimore and G. R. Heal, *J. Colloid Interface Sci.*, 42 (1973) 2, 233.
25 Y. Morioka, J. Kobayashi and I. Higuchi, *J. Colloid Interface Sci.*, 42 (1973) 1, 156.
26 A. P. Karnaukhov, *Pore Structure and Properties of Materials*, Vol. 1, Akademia, Prague, 1973, pp. A3–33.